



ELSEVIER

Tectonophysics 350 (2002) 127–156

TECTONOPHYSICS

www.elsevier.com/locate/tecto

# Seismic reflectivity of detachment faults of the Iberian and Tethyan distal continental margins based on geological and petrophysical data

Andreas B. Hölker<sup>a,\*</sup>, Klaus Holliger<sup>a</sup>, Gianreto Manatschal<sup>b</sup>, Flavio Anselmetti<sup>a</sup>

<sup>a</sup>*Department of Earth Sciences, Swiss Federal Institute of Technology, ETH-Zentrum, CH-8092 Zurich, Switzerland*

<sup>b</sup>*CGS-EOST, CNRS–Université Louis Pasteur, F-67084 Strasbourg, France*

Received 15 May 2001; accepted 11 March 2002

## Abstract

Low-angle detachment faults are key to our understanding of the tectonic evolution of magma-poor rifted continental margins. In seismic images of present-day rifted margins the identification and interpretation of such features is, however, notoriously difficult and ambiguous. We address this problem by studying the structure and seismic response of such faults through a synoptic interpretation of petrophysical data and geological evidence from the distal segments of the present-day West Iberian and the ancient Tethyan margins. On the basis of the geologically well-constrained remnants of the Tethyan margins, which are spectacularly preserved and exposed in the Alps of Eastern Switzerland, vertical profiles at four key geological settings of a typical magma-poor rifted margin are constructed and their synthetic seismic responses are compared to the observed seismic data from corresponding locations in the present-day Iberian margin. The seismic structure of these profiles is considered as the sum of deterministic large-scale and the stochastic small-scale components. Both components are analyzed for all pertinent lithologies. The large-scale structures are derived from laboratory measurements on samples from both, the West Iberian and Tethyan margins, whereas the small-scale fluctuations are constrained predominantly on the basis of well-log data from the Iberian margin. Different realizations of the simulated stochastic small-scale velocity fluctuations illustrate the potential variability of impedance contrasts and its impact on the seismic response from lithological interfaces and fault structures. Our results indicate that the nature of the seismic response from low-angle detachment faults is largely determined through the fracture-healing behavior of the surrounding rocks. Geological evidence from the exposed fragments of the Tethyan margins indicate that fracture-healing is generally well developed in crustal lithologies, but largely absent in mantle lithologies. It is for this reason that low-angle, intra-crustal detachment faults tend to be seismically undetectable. Conversely, crust–mantle detachments have a complex and variable seismic response, depending on the nature of the damaged zone and on the frequency content of the seismic data. These model-based inferences are consistent with the available evidence from the present-day Iberian passive margin and thus open new perspectives for the interpretation of the corresponding seismic images. © 2002 Elsevier Science B.V. All rights reserved.

*Keywords:* Rifted margins; Detachment faults; Seismic structure; Statistical analysis; Seismic models; Physical properties

\* Corresponding author.

*E-mail address:* hoelker@erdw.ethz.ch (A.B. Hölker).

## 1. Introduction

For more than a decade, magma-poor rifted continental margins have been extensively investigated for their architecture and tectonic evolution. The research focused on both, present-day margins, like that west of Iberia (e.g., Boillot et al., 1995; Reston et al., 1996; Whitmarsh et al., 2000), as well as preserved fragments of ancient counterparts, like those of the former Mesozoic Tethys (e.g., Froitzheim and Eberli, 1990; Bertotti et al., 1993; Froitzheim and Manatschal, 1996; Manatschal and Nievergelt, 1997). Of particular interest are the architecture and tectonic evolution of the distal segment of such margins, because they record the transitional period between rifting and seafloor spreading. In these areas, shallow low-angle detachment faults separate different crustal units, exhume subcontinental mantle at the ocean–continent transition (OCT), and accommodate extension during late stages of rifting (Manatschal and Bernoulli, 1999). Such detachment faults are notoriously difficult to identify on seismic images of the present-day margins and contrasting interpretations exist (e.g., Krawczyk et al., 1996; Whitmarsh et al., 2000; Manatschal et al., 2001). In contrast, detachment structures are well preserved and geometrically well defined in the Alps of eastern Switzerland (Florineth and Froitzheim, 1994; Manatschal and Nievergelt, 1997).

The West Iberian margin has been extensively imaged and studied through geophysical methods, mostly reflection seismic surveys (e.g., Mauffret and Montadert, 1987; Krawczyk et al., 1996; Reston et al., 1996), and was the object of four ocean drilling legs (Deep Sea Drilling Project (DSDP) Leg 47B; Ocean Drilling Program (ODP) Legs 103, 149 and 173). Recently, the deep seismic structure was investigated on the basis of refraction seismic surveys (e.g., Chian et al., 1999; Dean et al., 2000). Conversely, the architecture and tectonic evolution of former Tethyan margins have been reconstructed largely based on field observations (e.g., Froitzheim and Eberli, 1990; Bertotti et al., 1993; Florineth and Froitzheim, 1994; Manatschal and Nievergelt, 1997), but also on thermo-mechanical modeling (Bertotti et al., 1999). Recently, Manatschal and Bernoulli (1999) compared the West Iberian and Tethyan–Adriatic margins on the basis of stratigraphic, structural, petrological, and geo-

chronological data. Among other aspects, their efforts focused on the role of detachment faulting in mantle exhumation and in the formation of an OCT. However, no attempt was undertaken so far to synthesize the seismic structure of the ancient and present-day margins.

In this study, we pursue two aims: (i) to provide a comprehensive database describing the velocity and density structure of the pertinent lithologies in the distal segment of the West Iberian and two Tethyan margins; and (ii) to investigate the seismic responses of shallow detachment faults on the basis of synthetic seismograms. In contrast to mylonitic shear zones, whose seismic nature was investigated by, e.g. Jones and Nur (1982), McCaffree and Christensen (1993), Fountain et al. (1984), and Hurich et al. (1985), this work investigates the seismic nature of detachment faults in the brittle regime. We first outline the geological setting of four key situations across a distal margin and an OCT. For this purpose vertical tectono-stratigraphic profiles, which are exposed and well constrained, are constructed for the Tethyan margins, representing the situation after rifting but before Alpine orogeny. Their evolutionary stage corresponds to that of a mature margin such as that encountered today west of Iberia. Next, the seismic velocity and density structures of these profiles are analyzed based on laboratory data and wire-line logs from the Iberian margin and laboratory data from the Tethyan margins. Finally, 1D velocity and density models are constructed and synthetic seismograms are computed in order to evaluate the seismic response of the detachment structures. In doing so, we emphasize the role of small-scale velocity fluctuations and their effect on the seismic response in both analysis of the velocity structures and subsequent modeling. The resulting synthetic seismograms are finally discussed with reference to survey data from the West Iberian margin (Lusigal 12 profile, e.g. Beslier, 1996).

## 2. Geologic setting and lithological profiles

We use four exposed tectono-stratigraphic profiles from well preserved fragments of the ancient Tethyan margins in the Alps of eastern Switzerland as the geological base of this study. Profiles A and B are from the Jurassic to Cretaceous Tasna OCT, which belonged

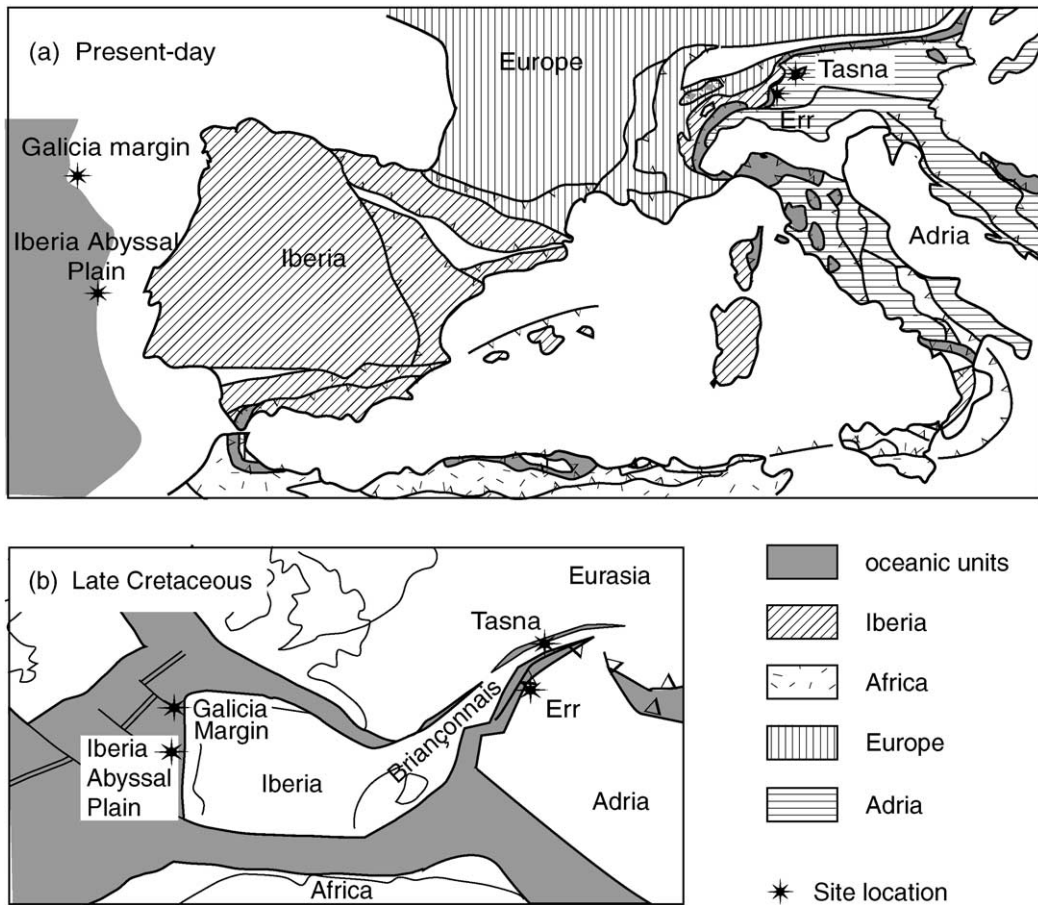


Fig. 1. (a) Schematic tectonic map of SW Europe showing the locations of Err, Tasna, Galicia margin and Iberia Abyssal Plain. (b) Paleogeographic map for the Late Cretaceous. From Manatschal and Bernoulli (1999).

to the Briançonnais margin (Florineth and Froitzheim, 1994) (Figs. 1 and 2). Profiles C and D represent two situations in the Jurassic Err detachment system, which belonged to the distal margin of Adria (Froitzheim and Eberli, 1990; Froitzheim and Manatschal, 1996; Manatschal and Nievergelt, 1997) (Figs. 1 and 2). Both settings are preserved within Alpine thrust sheets, in which the metamorphic overprint never exceeded low- to medium-temperature greenschist facies. Moreover, these thrust sheets show only little internal deformation, so that the geometries of the Mesozoic detachment systems can be restored with confidence. The profiles (Fig. 3) are described and compared to three analogous sites along the West Iberian margin (ODP Sites 639, 1067, and 1068 in Fig. 4). A synopsis of the considered margins is shown in Fig. 2.

### 2.1. Ocean–continent transitions: Profiles A, B; Sites 1068, 1067

The Tasna OCT is so far the only known place in the Alps where the lateral transition from continental crust to exhumed serpentinized mantle lithosphere is exposed and not disrupted by Alpine thrusting. The outcrop extends over a length of 5 km along a mountain ridge (Florineth and Froitzheim, 1994). The general structure of the Tasna OCT shows a wedge of continental crust thinning oceanwards (Fig. 2d). It is bounded by two detachment faults, the Upper Tasna Detachment (*UTD*) and the Lower Tasna Detachment (*LTD*) (Froitzheim and Rubatto, 1998). The *LTD* separates crustal rocks in the hanging wall from serpentinized mantle rocks in the footwall and is cut by the

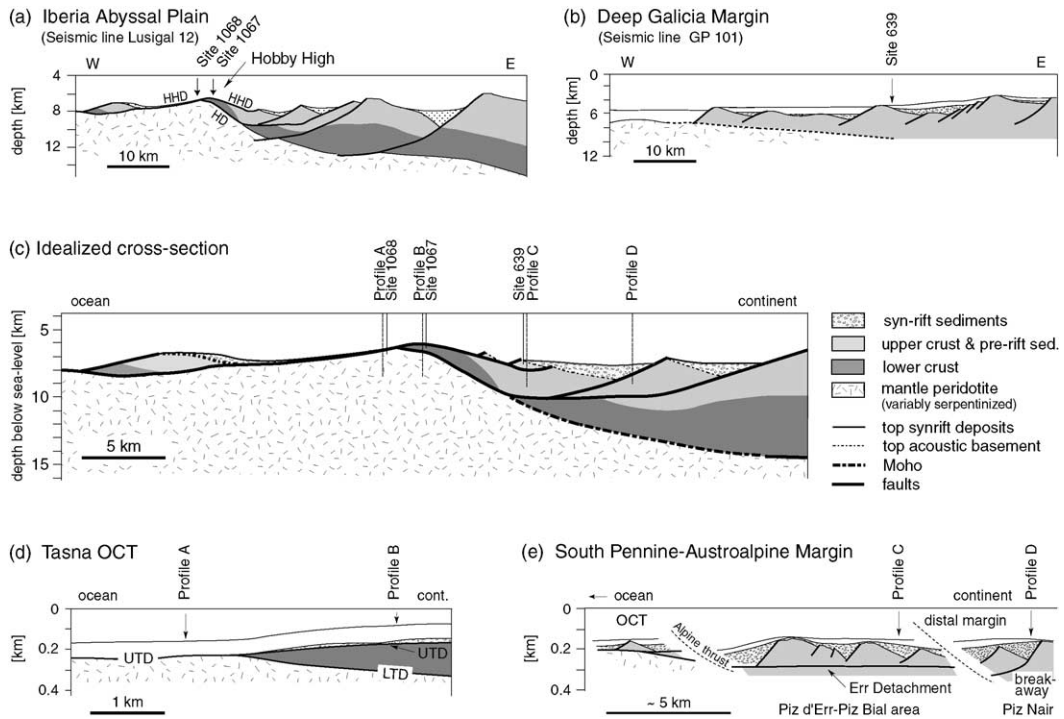


Fig. 2. Synopsis of the West Iberian and Tethyan margins: (a) Iberia Abyssal Plain (Manatschal et al., 2001), (b) deep Galicia Margin (Boillot et al., 1988), (c) an idealized cross-section across a magma-poor margin, showing the hypothesized locations of the studied profiles, (d) Tasna OCT (modified after Florineth and Froitzheim, 1994), and (e) Err detachment system (Manatschal and Nievergelt, 1997). *HHD* and *HD* refer to the Hobby High Detachment and the proposed H-Detachment. *UTD* and *LTD* refer to the Upper and Lower Tasna Detachment.

*UTD*, which forms the top of the continental crust on the continentward side and the top of the serpentinized mantle on the oceanward side. The *UTD* is stratigraphically overlain by black shales. These are post-rift sediments and seal the detachment faults. The overall situation at Tasna compares well with Hobby High in the Iberia Abyssal Plain (Whitmarsh et al., 2000). At Hobby High, continental basement rocks have been drilled at Sites 900 and 1067 and serpentinized mantle was recovered at Site 1068. These sites are less than 2 km apart from each other and covered by post-rift sediments. Based on seismic profiles and ODP data, Manatschal et al. (2001) interpreted Hobby High to represent a wedge of continental crust bounded by two detachment faults, the H-Detachment (*HD*) separating the crustal rocks in the hanging wall from serpentinized mantle rocks in the footwall, and the Hobby High Detachment (*HHD*) forming the top of the continental crust and of the serpentinized mantle (Fig. 2a). In

contrast to the *HHD*, the *HD* has never been drilled and its existence is postulated based on the interpretation of the seismic data, alone (Krawczyk et al., 1996; Whitmarsh et al., 2000).

In addition to the striking similarities in architecture, the lithologies observed in the Tethyan and Iberian OCTs are also quite similar. In both OCTs, serpentinized peridotite (*MI*, Table 4) represents the exhumed subcontinental mantle (Froitzheim and Rubatto, 1998; Hébert et al., 2001). In the Tasna OCT an increasing vein density towards the *LTD* within the serpentinized peridotite may record a pre-Alpine increase in fracture density towards the fault. At Site 1068, recovery in the mantle rocks increases downwards away from the tectonized top, which may be related to the downward decreasing fracture density (Whitmarsh et al., 1998, Fig. 2, p. 167). At the top of the serpentinized peridotite (*MI*) strongly brecciated serpentinite, commonly cemented by calcite

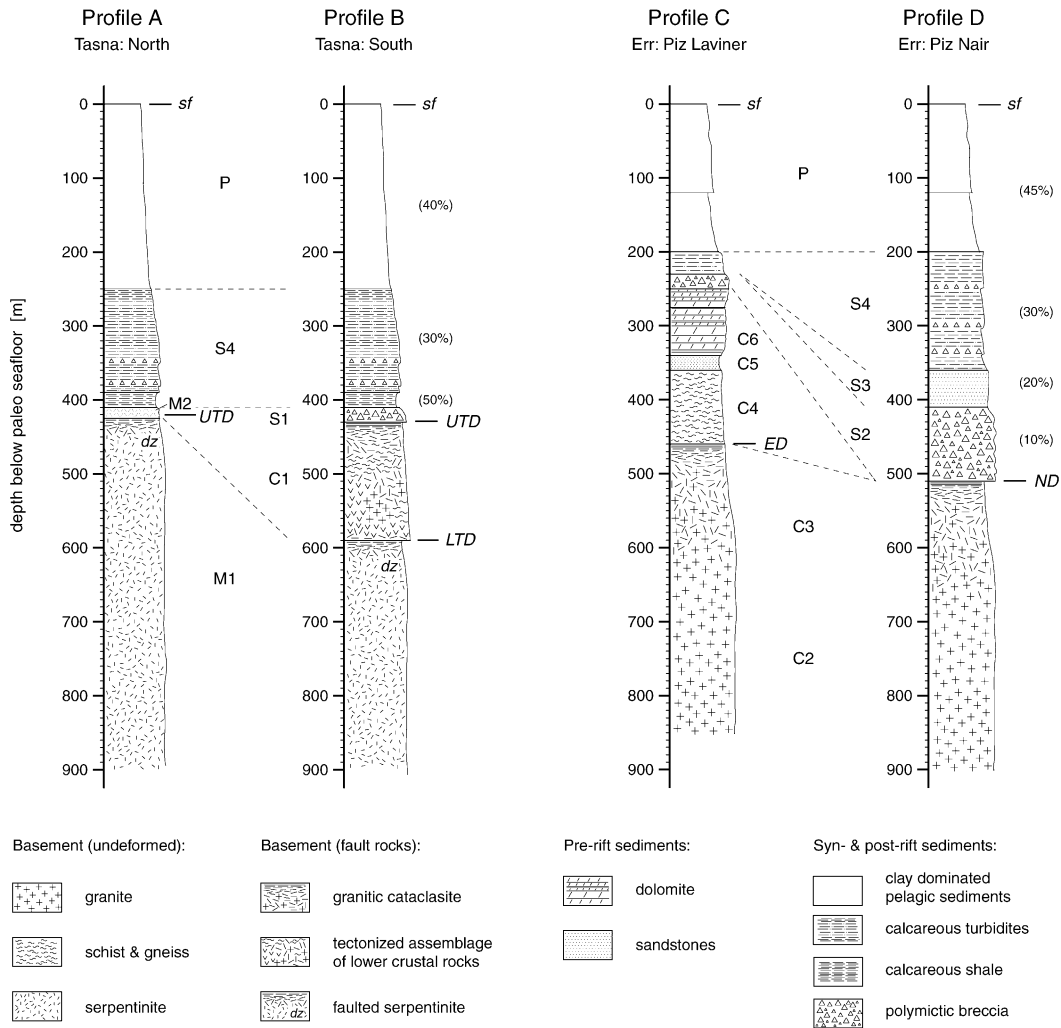


Fig. 3. Tectono-stratigraphic profiles of the former Tethyan margins preserved in the Err and Tasna thrust sheets. The location of these profiles within the overall tectonic framework is illustrated in Fig. 2. The abbreviations *UTD*, *LTD*, *ED* and *ND* refer to the Upper and Lower Tasna Detachment, the Err detachment and the breakaway at Piz Nair; *sf* is the seafloor and *dz* a damaged zone in the upper-most serpentinite. In order to compensate for compaction during Alpine history, the thickness of the sedimentary units has been increased according to assumed former porosities (percentage given in parentheses). Indices refer to the lithological units described in the text.

(ophicalcites), occurs in the Iberian margin as well as in Tasna. These ophicalcites (*M2*, Table 4) occur as a discontinuous layer of varying thickness and are associated with the detachment structures.

The Variscan continental crust in the Tasna OCT consists of a heterogenous and strongly tectonized assemblage of amphibolites, gabbros, tonalites, and migmatites (*C1*, Table 4). Locally, polymictic breccias

(*S1*, Table 4) with crystalline basement clasts occur along the top of the basement. Some of these breccias are the product of in situ fragmentation, others are of sedimentary origin. At Sites 900 and 1067, strongly tectonized amphibolites, gabbros, anorthosites, and tonalites were recovered (Fig. 4). Their genesis and exhumation history compares closely with that of the crustal rocks preserved in the Tasna OCT (L. Desmurs,

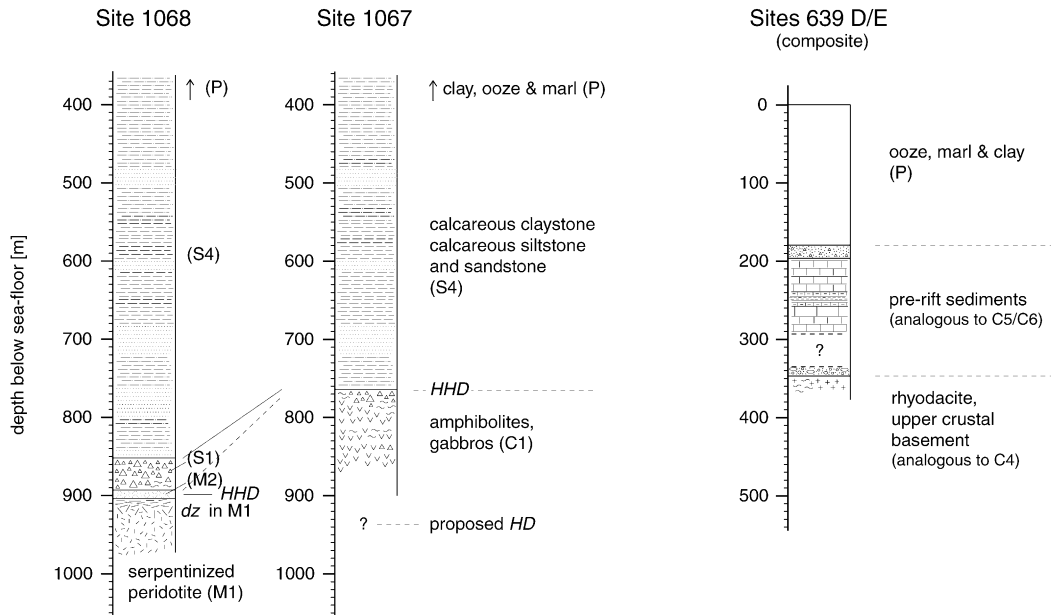


Fig. 4. Lithological profiles from Sites 1068, 1067, and 639 corresponding to the profiles from the former Tethyan margins in Fig. 3. *S1* are polymictic breccias, *M2* are ophiolites, *dz* is the damaged zone below the Hobby High Detachment (*HHD*) and *HD* is a proposed detachment fault leading to the H-reflector. Data from Boillot et al. (1987), Sawyer et al. (1994), Whitmarsh et al. (1998).

personal communication). Further oceanwards, at Site 1068, sedimentary breccias overlie the serpentinized mantle. Similar breccias overlying the mantle rocks are locally observed in the Tasna OCT but are not included in Profile A.

Post-rift sediments unconformably overlie both, the present-day Iberian and the former Tethyan OCTs. In the Tasna OCT, the oldest post-rift sediments consist of a thin layer of shales. They are overlain by fine-grained calcareous turbidites (*S4*, Table 4) which are interbedded with minor breccia layers. In Iberia, the post-rift sequence is formed by claystones, calcareous silt- and sandstones (*S4*). The late post-rift evolution is different in the two OCTs. While the Iberia Abyssal Plain remained in a deep marine environment, the late post-rift sequence in the Tasna OCT records also Alpine convergence. For this reason we did not investigate the late post-rift sediments in Tasna and replaced them in our velocity and density models by the late post-rift sedimentary sequence of the Iberia margin (*P*). Profiles A and B in Fig. 3 and the profiles of Sites 1067 and 1068 in Fig. 4 summarize the continentward and oceanward side of the OCT, respectively.

## 2.2. Distal margin: Profiles C, D; Site 639

The Err detachment and the breakaway at Piz Nair are parts of a crustal-scale detachment system, composed of several low-angle detachment faults (Froitzheim and Eberli, 1990; Manatschal and Nievergelt, 1997). These faults developed during a late stage of rifting and show a top-to-the-ocean sense of shear. They separate continent-derived blocks of variable size from continental crust in the footwall and are commonly associated with tectonic and tectono-sedimentary breccias. The overall structure has been compared with shallow crustal reflections on seismic profiles from the Iberian margins (Manatschal and Bernoulli, 1999). On a margin scale, the detachment system in the Err and the Iberian margins form breakaways in the continental crust.

We present two profiles from the Err detachment system (Fig. 3). Profile C at Piz Lavinér summarizes the situation across a tilted block resting on the Err detachment and Profile D at Piz Nair shows the detachment fault overlain by a sequence of syn-rift sediments. The footwall of the Err detachment fault in Profile C consist of a green, granitic cataclasite

(C3, Table 4) which grades downwards into a homogeneous granite (C2, Table 4). The fault plane itself is marked by a black fault gouge and the fault rocks were healed during rifting by precipitation of  $\text{SiO}_2$  derived from the breakdown reaction of feldspar (Manatschal, 1999). The thickness of the macroscopically damaged zone accompanying the detachment fault is in the order of 100–150 m.

The tilted block forming the hanging wall in Profile C is formed by an assemblage of polymetamorphic schists and gneisses (C4, Table 4), which are unconformably overlain by a sequence of Permo-Triassic to Liassic pre-rift sediments (Naef, 1987). The pre-rift sediments can be subdivided, broadly, into continental clastics (C5, Table 4) which are overlain by shallow-water dolomites (C6, Table 4). Syn-rift deposits unconformably overlie the pre-rift sediments and consist of sandstones intercalated with breccia layers (S2, Table 4). They grade upwards into a sequence of fine-grained calcareous turbiditic sandstones and siltstones interbedded with layers of hemipelagic claystones (S4). The post-rift sediments consist of radiolarian cherts, which are overlain by pelagic limestones intercalated with shales. As in the Tasna profiles, late post-rift sediments are replaced by the late post-rift sedimentary sequence of the Iberian margin (P).

Profile D across the breakaway at Piz Nair represents a particularly well exposed syn-rift sequence consisting of (i) coarse grained breccias at the base (S2), overlain by (ii) sandstone dominated series with minor breccia layers (S3, Table 4) and (iii) a sequence of fine-grained calcareous turbiditic sandstones and siltstones interbedded with layers of hemipelagic claystone (S4) which are overlain by a post-rift sequence consisting of radiolarian cherts and hemipelagic to pelagic limestones and shales (Finger, 1978). Although the Piz Nair syn- to post-rift sedimentary sequence has been deformed during Alpine convergence, its primary contact to the basement is locally preserved and the overall structure of the breakaway can be restored (Froitzheim and Manatschal, 1996). Thus, Profile D shows a section across the detachment fault with syn- and post-rift sediments sealing the fault zone. The basement rocks consist of granites which show a strong cataclastic deformation towards the detachment fault, very similar to the situation described from the footwall of the Err detachment in Profile C.

The syn-rift deposits (S2) contain clasts of the pre-rift sediments (C5 and C6) and all basement lithologies including the cataclasites (C3) derived from the detachment faults itself. This shows that the pre-rift sediments were well lithified when rifting started. Evidence for syn-tectonic fracture healing in cataclasites, associated with the Err detachment, are shown and discussed by Manatschal (1999, Fig. 5h).

ODP Site 639 in the distal Galicia margin is considered to represent a situation analogous to the upper part of Profile C. It is interpreted as the top of a tilted block (Boillot et al., 1987, p. 411). At this site, several drill holes (639 A–F) penetrated a series of pre-rift sediments. Unfortunately, drilling stopped near the very top of the acoustic basement and sampled only the uppermost continental basement, which consists of volcanics including rhyodacites. On the seismic line GP101 (Mauffret and Montadert, 1987), the tilted block is soled by a reflection known as the S-reflector which was interpreted by Boillot et al. (1995) and Reston et al. (1996) as a low-angle detachment fault. This reflection is imaged at 1.5-s two-way travel time below the top of the acoustic basement. Structures occurring at this depth are not observable in the Err thrust sheet, which is less than 500 m thick. The Err detachment is clearly a very shallow crustal structure as indicated by the juxtaposition of pre-rift sediments against basement rocks as well as the local exposure of the detachment fault at the seafloor which is indicated by syn-rift sediments sealing the detachment surface (Manatschal and Nievergelt, 1997).

### 3. Large-scale velocity and density structures and velocity distributions

The aim of the following two sections is the characterization of seismic velocity and bulk density structures of the pertinent lithological units in the Alpine and Iberian sites. The velocity–depth structure  $V(z)$  of each unit is described as the sum of a large-scale deterministic component  $V_0(z)$  and small-scale stochastic fluctuations  $\Delta V(z)$  (Holliger, 1996):

$$V(z) = V_0(z) + \Delta V(z) \quad (1)$$

In this section, we investigate the large-scale velocity trend  $V_0(z)$  as well as the magnitude and

distribution of the fluctuations around this trend. A corresponding model is used for the density structure  $\rho(z)$ . Both the large-scale trend and the small-scale fluctuations are considered to be distinct for each lithological unit.

### 3.1. Velocity and density data from the Iberia Abyssal Plain and the Galicia Margin

Data from the Iberian sites are available from ODP Legs 103, 149 and 173 (Boillot et al., 1987; Sawyer et al., 1994; Whitmarsh et al., 1998) either as in situ measurements in boreholes (wire-line logs) or as discrete measurements on samples which were recovered from boreholes (laboratory measurements). In the following subsections, the results of the serpentized peridotites as well as of the syn- and post-rift sediments are discussed in detail, because their seismic structure is more complex than those of the other units. The results of these remaining units are summarized in Table 1.

#### 3.1.1. Serpentized peridotite (M1)

Serpentized peridotites (M1) were drilled at Site 637 off Galicia and at Sites 897, 899, 1068, and 1070 in the Iberia Abyssal Plain. Laboratory measurements and sonic log data show a steep increase of sonic velocity with depth and strong velocity fluctuations within the uppermost 100 m of the serpentinite. Drill-core observations show that the uppermost M1 is

Table 1

Average velocities  $\bar{V}$  and densities  $\bar{\rho}$  in polymictic breccias, tectonized lower crustal rocks (CI), and ophicalcite in the Iberian margin

Unit	Lithology	$\bar{V} = V_0(z)$ [m/s]	$\sigma_V$ [m/s]	$\bar{\rho} = \rho_0(z)$ [kg/m <sup>3</sup> ]	$\sigma_\rho$ [kg/m <sup>3</sup> ]
S1	polymictic breccias	4889	819	2630	170 <sup>a</sup>
CI	amphibolites, gabbros	5700	777	2780	160 <sup>a</sup>
–	felsic volcanics	6310	–	2800	– <sup>b</sup>
M2	ophicalcite	4437	737 <sup>c</sup>	2540	140 <sup>a</sup>

$\sigma_V$  and  $\sigma_\rho$  are the standard deviation of velocity and density, respectively.

For velocities of units P, S4, S3, S2 and M1, see the text and figures.

<sup>a</sup> Based on discrete samples (laboratory measurements).

<sup>b</sup> Measurements on only two samples available.

<sup>c</sup> See Fig. 6b.

Table 2

Large-scale velocity and density model of serpentized peridotite at Sites 637, 899 and 1068

	<i>A</i>	<i>a</i>	<i>B</i>	<i>b</i>
$V_0$	4208	0.1	327	0.1
$\sigma_V$	600	0.14		
$\rho_0$	2522	0.005	500	0.001

The parameters *A*, *a*, *B* and *b* refer to Eqs. (2) and (3). Resulting units are m/s and kg/m<sup>3</sup>.

cataclastically deformed forming a damaged zone in the footwall of the detachment faults (see *dz* in Fig. 4, Site 1068). The transition from fractured to undeformed rocks explains the significant velocity increase within the uppermost M1.

Velocity–depth gradients at a depth range from 500 to 3000 m below the top of the basement, as derived from wide-angle seismic data by Chian et al. (1999), are much smaller than in the damaged zone. In order to describe the average velocities at shallow and deeper depth, the following model (modified after Wepfer and Christensen, 1991) was used:

$$V_0(z) = A \left( \frac{z}{100} \right)^a + B(1 - e^{-bz}), \quad (2)$$

where  $V_0$  is the seismic velocity,  $z$  is depth below the detachment fault and *A*, *a*, *B* and *b* are adjustable parameters. Bulk densities in the serpentized peridotite can be described by an analogue relation (Table 2 and Fig. 5).

The probability distribution of velocity fluctuations in the damaged zone can be well approximated by Gaussian distribution (Fig. 6a). At Sites 637, 899, and 1068, standard deviations of velocity up to 500 m/s were observed within the damaged zone. For a depth range of 2000–6000 m below the top of the serpentinites, standard deviations of 200 m/s were estimated by Chian et al. (1999). A power law relation

$$\sigma_V(z) = Az^{-a} \quad (3)$$

can be used to approximate standard deviation of velocity  $\sigma_V$  in the entire interval, where  $z$  is depth below the detachment fault and *A* and *a* are adjustable parameters.

#### 3.1.2. Syn-rift sediments (S2 and S3)

Sandy turbidites and hemipelagic sediments interpreted as syn-rift deposits (Boillot et al., 1988) and

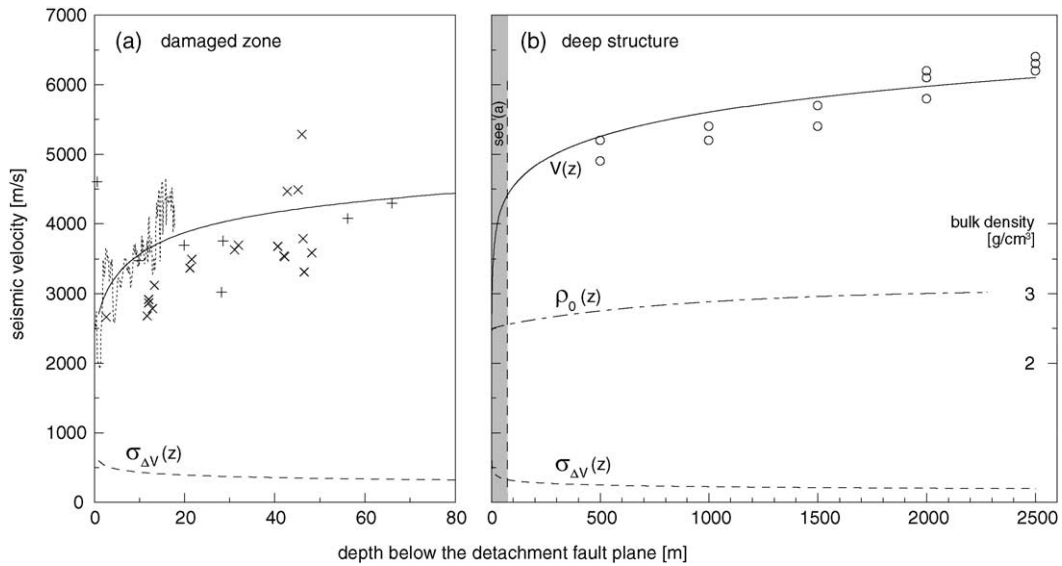


Fig. 5. Large-scale velocity and density model for the serpentinite: (a) damaged zone at shallow depth below a detachment fault, (b) entire model based on seismic refraction data. Solid lines represent the velocity depth model, dashed lines the standard deviation, and dashed–dot line bulk density. Crosses and the dotted line denote sonic velocity data from Sites 637, 899 and 1068 and circles are velocity constraints at greater depth taken from Chian et al. (1999). The corresponding models and parameters are given in Eqs. (2) and (3) as well as in Table 2.

recovered at Sites 638 and 639 consist of two lithologies: unconsolidated clay and cemented sandstone. According to shipboard measurements, the soft sediments have a velocity–depth gradient ( $dV/dz$ ) of  $0.8 \text{ [m/s m}^{-1}\text{]}$  and  $V(0) = 1443 \text{ m/s}$  (with  $z=0$  referring to the seafloor). The standard deviation  $\sigma_V$  of the soft

sediments is  $109 \text{ m/s}$  in the depth interval ranging from  $300$  to  $550 \text{ m}$  below seafloor. A velocity–depth gradient in the cemented sandstones can not be determined in the considered interval. Their mean velocity and standard deviation are  $\bar{V} = 3996 \text{ m/s}$  and  $\sigma_V = 580 \text{ m/s}$ . Bulk density in the unconsolidated material is  $\bar{\rho} = 2140$

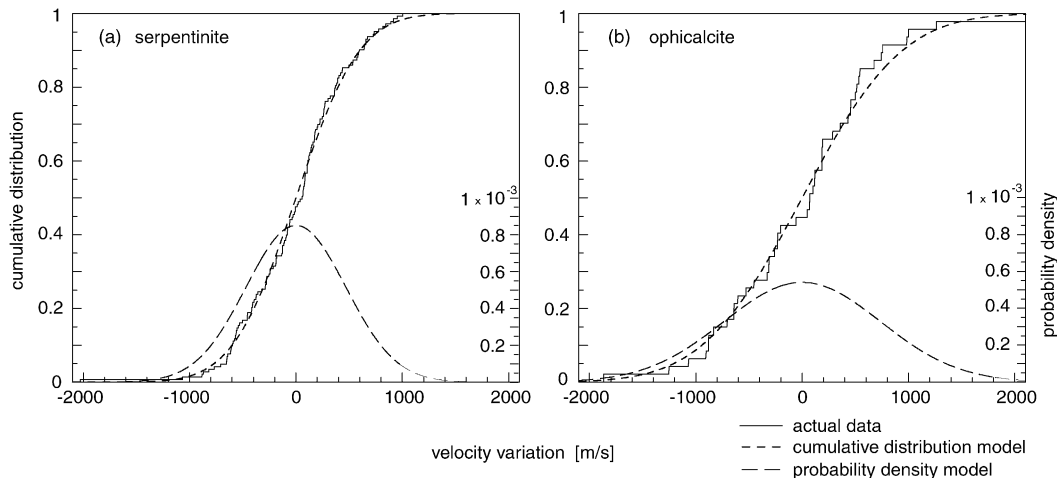


Fig. 6. Cumulative distribution and probability density function of velocity fluctuations in (a) serpentinitized peridotite and (b) ophicalcite. The solid lines represent the actual data and the dashed lines the best-fitting Gaussian models: the cumulative distribution function (short dashed line) and the corresponding probability density function (long dashed line).

and  $\sigma_p = 120 \text{ kg/m}^3$ , respectively  $\bar{\rho} = 2660$  and  $\sigma_p = 120 \text{ kg/m}^3$  in the cemented sandstones. For comparison, velocities up to 4000 m/s were obtained from wide-angle seismic data for the deepest parts of the basins (Chian et al., 1999).

### 3.1.3. Post-rift sediments (*S4* and *P*)

Fine-grained calcareous turbidites (*S4*) grade upwards into chalk- and clay-dominated sediment (*P*). While all *P* and the clayey sediments of *S4* are unconsolidated, partial lithification occurs at greater depth in the silty and sandy beds of *S4*. These lithified beds cause the high velocity peaks at depth below 640 m in Fig. 7. The probability distribution of velocity fluctuations in the totally unlithified material is Gaussian (Fig. 8a) whereas the overall distribution in the partially lithified interval is better approximated by log-normal distribution (Fig. 8b).

Sonic velocities in the sediments are 1500 m/s at the seafloor and linearly increase with depth. A velocity gradient of  $1 \text{ m/s m}^{-1}$  was obtained for both units (*S4* and *P*) at Site 900 (Hobby High) where 700 m of post-rift sediments have been continuously sampled. Measurements on samples from Sites 897, 898, 899, 1065, 1067, 1068, 1070 and a sonic log from Site 637 are consistent with this trend as shown in Fig. 7.

The variance of velocity fluctuations increases with depth in the unlithified sediment. This might be an effect of a varying degree of consolidation in the indi-

vidual beds, which rises with depth of burial. In order to quantify this effect, standard deviation was calculated as function of depth and approximated by a linear trend as illustrated in Fig. 9.

The shifted log-normal distribution model of the deeper sediments (Fig. 8b) adequately fits velocity variations between +200 and +2600 m/s. Above and below there are deviations from the model, which are considered to be sampling artifacts. The parameters quantifying the distributions of small-scale velocity fluctuations are compiled in Table 3.

### 3.2. Velocity and density data from the Alpine sites: *Err* and *Tasna*

Velocity and density data from the Alpine sites were obtained from measurements on 225 rock samples which were collected as hand-specimens or mini-plugs. Because of the Alpine topography it was not always possible to sample along vertical profiles and sampling rather focused on adequately covering all lithological units and their typical facies variations. Therefore, the statistical analysis of velocity fluctuations of these data is less rigorous compared to those from the Iberian sites. In order to simulate burial conditions, compressional wave velocity measurements were performed under increasing effective pressure conditions (Appendix A). The resulting velocity–pressure data are summarized for each lithological unit by the least-square

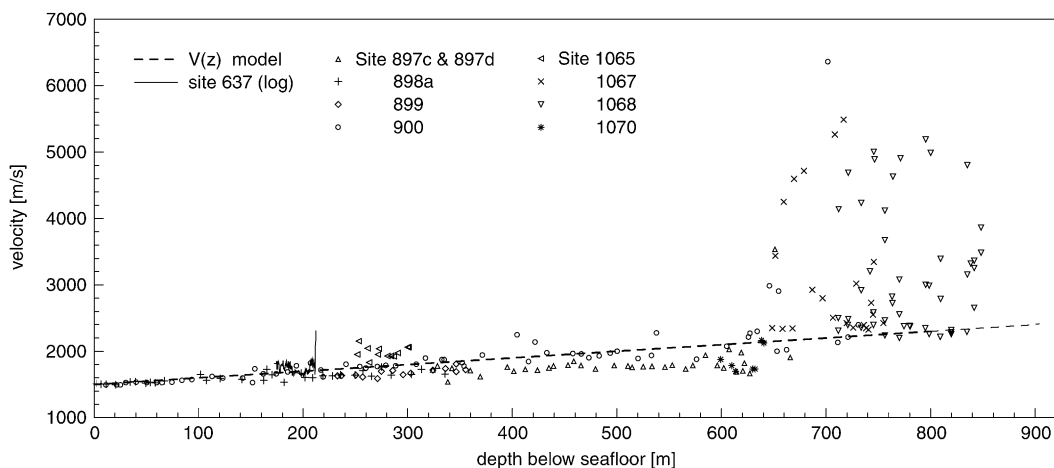


Fig. 7. Velocity–depth relation as observed in post-rift sediments in the Iberian margin. Note the high velocities occurring at depth below 640 m, which are caused by partial lithification. Data from ODP Legs 149 and 173.

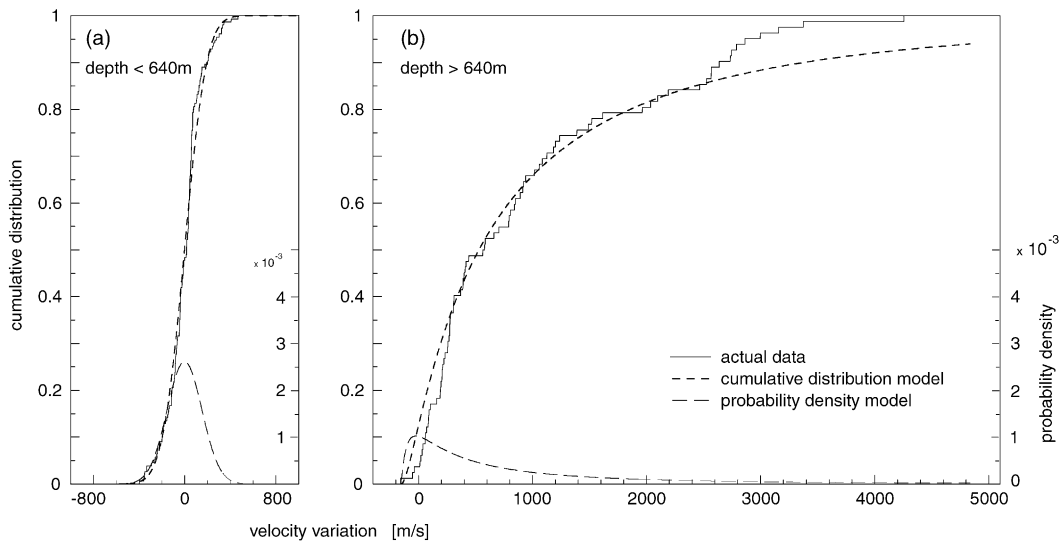


Fig. 8. Cumulative distribution and probability density function of velocity fluctuations in post-rift sediments: (a) unlithified sediment at depth shallower than 640 m below seafloor and (b) the partially lithified sediment at depth deeper than 640 m. The solid lines represent the actual data and the dashed lines the best-fitting Gaussian models: the cumulative distribution function (short dashed line) and the corresponding probability density function (long dashed line). The parameters quantifying both distributions are compiled in Table 3.

best-fit to the empirical model proposed by Wepfer and Christensen (1991):

$$V_0(P) = A \left( \frac{P}{100} \right)^a + B(1 - e^{-bP}), \quad (4)$$

where  $V_0$  is the average sonic velocity,  $P$  the effective pressure and  $A, a, B, b$  are adjustable parameters (Table

4; Fig. 10). Velocities, standard deviations of velocity and the velocity–pressure gradients were calculated for effective pressures of 1, 10 and 100 MPa from the model and the residual experimental data. These data are given together with the bulk densities in Table 5. The bulk density was determined based on measurements of weight and connected porosity (Appendix A).

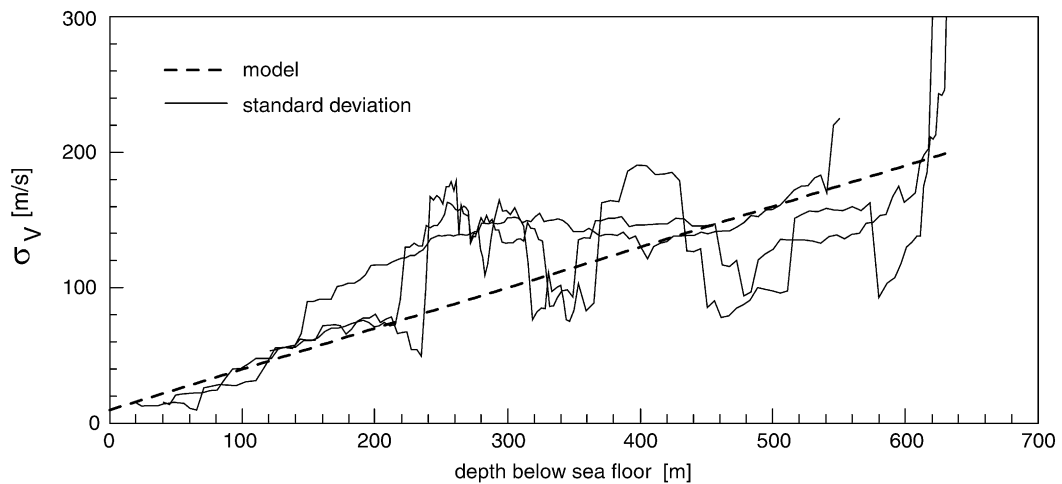


Fig. 9. Standard deviation calculated in moving windows for post-rift sediments at depth shallower than 640 m (solid lines) and a linear best-fitting model (dashed line).

Table 3  
Velocity and density models for sediments at ODP Sites 897, 898, 899, 900, 1065, 1067, 1068, 1070

	Depth < 640 m	Depth > 640 m
Velocity	$V_0(z) = z + 1500$ [m/s]	
Velocity distribution	normal	log-normal
	$\sigma_V(z) = 0.3 \cdot z + 10$ [m/s]	$\sigma_y = 1.276$ $\mu_y = 6.534$ shifted by – 160 m/s
Density	$\rho_{\text{bulk}}(z) = 1.4 \cdot z + 1600$ [kg/m <sup>3</sup> ] $\sigma_\rho = 144$ [kg/m <sup>3</sup> ]	

$\mu_y$  and  $\sigma_y$  are the mean and standard deviation of a log-normal distribution, respectively.

### 3.3. Comparison of velocity and density data from the Alpine and Iberian sites

Overall, velocities and densities of the corresponding lithological units in the Iberian sites compare well with those from the Alpine sites. Significant differences due to Alpine overprint occur in the syn-rift and post-rift sediments, which are still unconsolidated in the Iberian margin, as well as in fracture dominated basement lithologies.

Serpentinized peridotite (*MI*) in Iberia is characterized by a damaged zone below the detachment faults (see *dz* in Fig. 4, Site 1068), which results in a low-velocity zone. An equivalent damaged zone was mapped in Tasna on the basis of healed fractures and serpentinite veins whose density increase towards the detachment faults (see *dz* in Fig. 3, Profiles A and B). *MI* velocities in the Alpine samples taken close to the detachment faults do not differ in mean velocity from those taken at greater distance. Moreover, a steep velocity–pressure gradient at low pressures, indicating a significant presence of micro-cracks, cannot be recognized in the Alpine data (see *MI* in Fig. 10). Therefore, we assume that fracture healing in serpentinized peridotite is an Alpine event and hence that sonic velocities measured on the Alpine samples are higher than in those from the Iberian margin.

Ophicalcite (*M2*) occurs along both margins as discontinuous layers at the top of serpentinite and underlying sediments and locally the continental allochthons. These ophicalcite layers are frequently as-

sociated with detachment structures. Replacement and cementation by calcite appears to be the only significant healing process in brecciated serpentinite with respect to seismic velocities. Differences in average velocities between the Iberian and Alpine ophicalcites (Tables 1 and 5) are most likely the result of Alpine fracture healing.

Lower crustal rocks (*CI*) in the Iberian margin and in Tasna have a very similar mean velocity (Tables 1 and 5). Comparing typical *CI* velocities ( $\bar{V} = 5700$  m/s and  $\sigma_V = 777$  m/s) with velocities in amphibolite from the lower crust of the Ivrea zone ( $\bar{V} = 6200$ ,  $\sigma_V = 300$  m/s in Kern and Richter, 1981; Burke and Fountain, 1990), the higher mean and lower standard deviation of the latter are noteworthy. Such differences may underscore the high tectonization of lower crustal rocks in the most distal parts of a margin during rifting, while such a pervasive tectonization did not affect the lower crustal rocks in more proximal parts of a margin like in the Ivrea zone.

Only a few samples of volcanic rocks representing the upper crustal basement were recovered in the Galicia margin. Local occurrences of felsic volcanics

Table 4  
Parameters corresponding to the model defined by Eq. (4) quantifying velocity–pressure relations in lithological units in the Err and Tasna outcrops

Unit	Setting	Lithology	<i>A</i>	<i>a</i>	<i>B</i>	<i>b</i>
S4b	post-rift	calcareous turbidites	5788	0.0005	667	0.0035
S4a	late syn-rift	calcareous turbidites	5793	0.0006	671	0.0036
S3	syn-rift	sandstones	5031	0.0001	483	0.0679
S2	syn-rift	breccias	5431	0.0175	485	0.0066
S1	syn-rift	polymictic breccia	5309	0.0175	386	0.0136
C6	pre-rift	dolomites	6392	0.0001	315	0.0194
C5	pre-rift	sandstones	5337	0.0097	157	0.1
C4	upper crust	schists and gneisses	5224	0.0001	908	0.0030
C3	upper crust	cataclasites	5219	0.0001	546	0.0073
C2	upper crust	granites	5764	0.0178	140	0.0176
C1	lower crust	mainly amphibolite	5713	0.0193	283	0.0052
M2	tectonized mantle	ophicalcites	5946	0.0036	427	0.0059
M1	exhumed mantle	serpentinites	5654	0.0001	616	0.0011

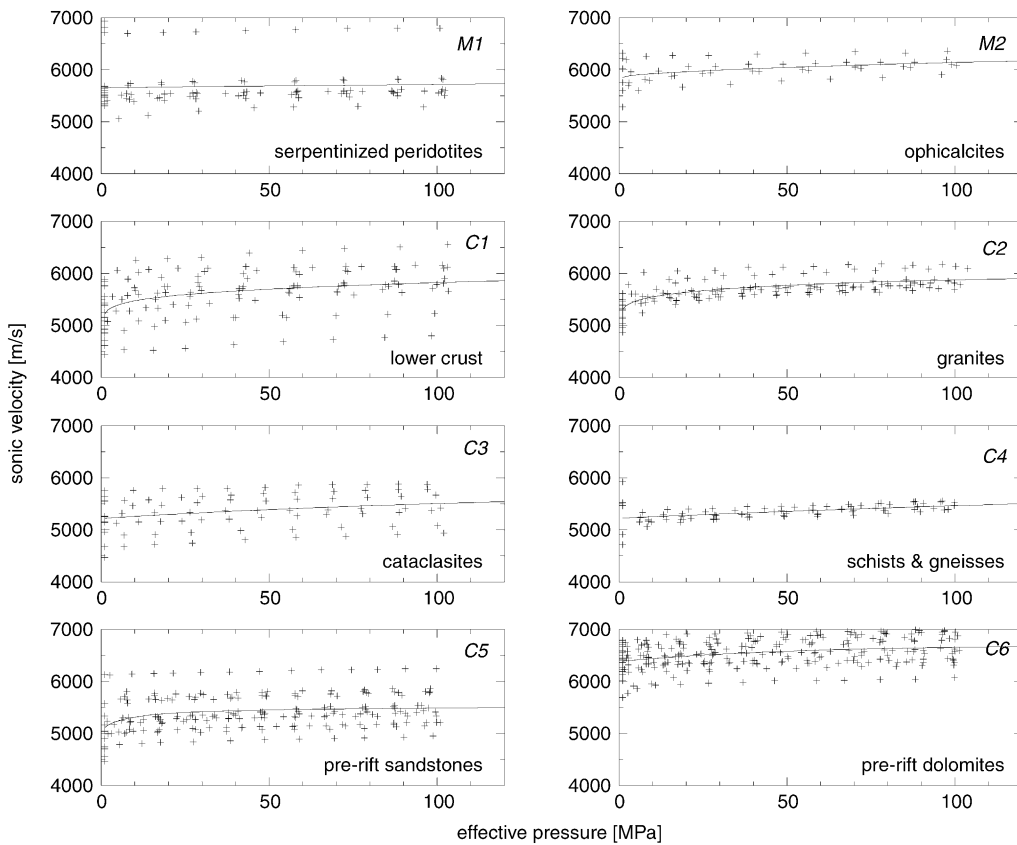


Fig. 10. Velocity data of the basement and pre-rift units for the Alpine sites. Crosses represent the experimental data and the solid line the best-fitting model according to Eq. (4).

are also known in *C4* in the Alpine sequences, but the dominant lithologies of continental upper crustal basement in the Err are granites (*C2*), cataclastic granites (*C3*), and an assemblage of gneisses and schists (*C4*). It is reasonable to directly use the velocities and densities of these lithologies for the modeling, because it can be assumed, that Alpine overprint did not seriously affect the acoustic properties of these rocks. This assumption also applies to the cataclastic granites (*C3*), because they were syn-tectonically healed (Froitzheim and Eberli, 1990).

Pre-rift sediments in the Galicia margin were not analyzed for two reasons: (i) their lithologies can not be directly compared with those in the Err and (ii) only scarce velocity data are available. Pre-rift sediments in the Tethyan margins must have been well lithified before rifting, because they occur as angular

clasts in syn-rift deposits. Just as for the cataclastic crustal rocks, their physical properties are therefore assumed not to have dramatically changed by Alpine overprint.

Velocity and density of the syn-rift polymictic breccias (*S1*) are identical in the Iberian and Alpine sites (Tables 1 and 4). Syn-rift sediments in a setting equivalent to *S2* in the Err have not been drilled in the west Iberian margin, because only basement highs were targeted by the drilling campaigns. In the deepest parts of the sedimentary basins seismic velocities up to 4000 m/s were interpreted from wide-angle seismic data (Chian et al., 1999). These velocities are clearly lower than those measured on *S2* samples from the Err. This indicates that a substantial part of compaction and lithification may have happened during Alpine overprint.

Table 5  
Average sonic velocities  $\bar{V}$  and bulk densities  $\bar{\rho}$  obtained from Alpine samples

Unit	Lithology	$\bar{V}$ [m/s]	$\sigma_V$ [m/s]	$dV/dP^a$	$\bar{V}$ [m/s]	$\sigma_V$ [m/s]	$dV/dP^a$	$\bar{V}$ [m/s]	$\sigma_V$ [m/s]	$dV/dP^a$	$\bar{\rho}$ [kg/m <sup>3</sup> ]	$\sigma_{\rho}$ [kg/m <sup>3</sup> ]
		at 1 MPa			at 10 MPa			at 100 MPa				
<i>S4b</i>	calc. turbidites	5777	362	4.3	5804	330	2.5	5982	271	1.7	2680	20
<i>S4a</i>	calc. turbidites	5778	249	5.0	5808	338	2.7	5996	291	1.7	2720	50
<i>S3</i>	sandstones	5060	177	30.0	5268	362	16.1	5513	467	0.04	2690	50
<i>S2</i>	breccias	5013	311	64.3	5247	173	11.7	5665	167	2.6	2740	50
<i>S1</i>	polymictic breccia	4902	614	65.5	5148	610	13.1	5596	555	2.3	2720	130
<i>C6</i>	dolomites	6395	262	6.4	6446	251	5.0	6662	265	0.9	2810	50
<i>C5</i>	sandstones	5119	497	47.9	5318	347	10.3	5494	323	0.5	2690	50
<i>C4</i>	schist and gneiss	5225	441	3.1	5250	97	2.7	5461	98	2.0	2700	30
<i>C3</i>	cataclasites	5220	404	4.3	5256	375	3.8	5503	373	1.9	2690	30
<i>C2</i>	granites	5312	213	68.4	5554	199	11.4	5880	165	1.4	2680	30
<i>C1</i>	amphibolite	5229	446	71.8	5479	474	11.4	5827	449	2.0	2760	140
<i>M2</i>	opicalcite	5850	363	17.3	5921	234	4.4	6137	161	1.6	2710	30
<i>M1</i>	serpentinite	5652	547	1.1	5659	421	0.7	5716	409	0.6	2680	110

*P* refers to effective pressure in this table.

<sup>a</sup>  $dV/dP$ : [m/s 1/MPa].

In the younger syn-rift and early post-rift sediments (*S3* and *S4*) differences in compaction and lithification by Alpine overprint are evident. While porosities in sediments of the present-day margin vary from 5% to 60% and velocities from 1500 to 5500 m/

s, the same primary lithologies in the ancient margin have now porosities of less than 5% and velocities ranging between 5200 and 6400 m/s. The good overall correlation between porosity and velocity documented in Fig. 11 suggests that velocity models of

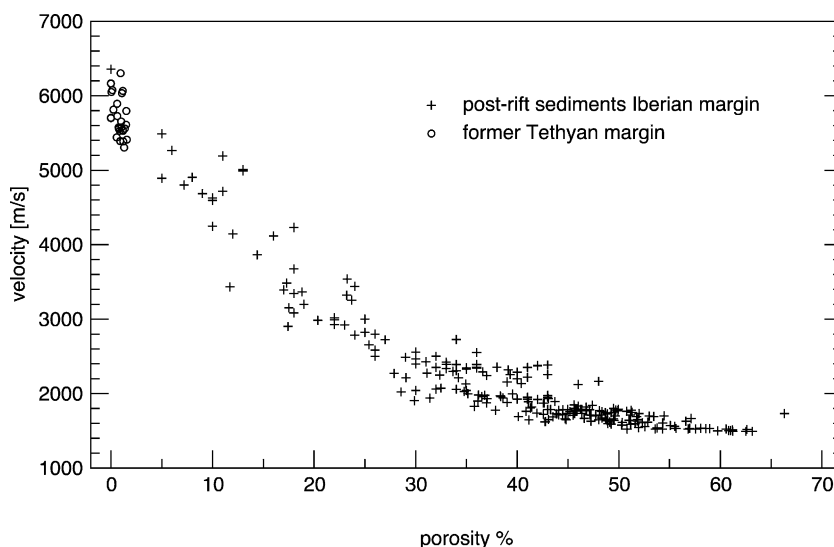


Fig. 11. Velocity–porosity relation in late syn-rift to post-rift sediments (units *S4* and *P*). Circles represent the strongly compacted samples from the former Tethyan margins preserved in the Alps and crosses represent the samples from the Iberian margin.

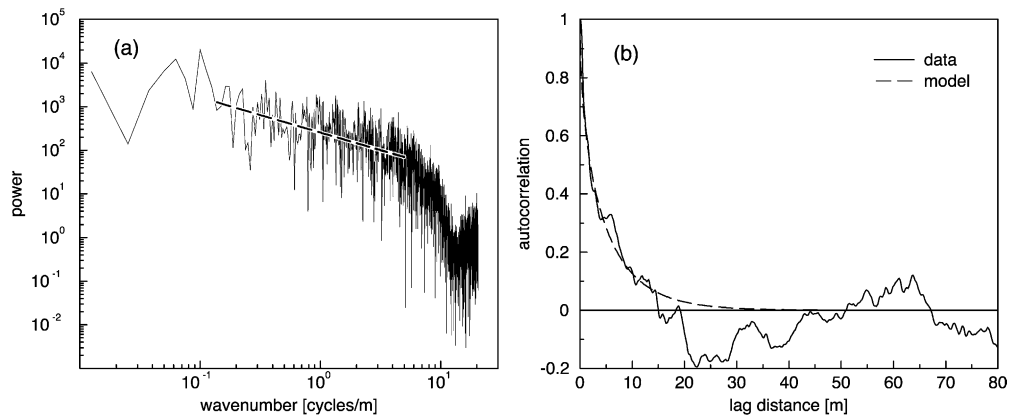


Fig. 12. (a) Power spectrum of bulk density fluctuations in post-rift sediments at ODP Site 1068. A preliminary value of  $\nu$  is estimated from the roll-off rate (dashed line) of the power-spectrum at intermediate wavenumbers. High wavenumbers have not been analyzed because they are dominated by the logging tool response. (b) Autocorrelation of the same log. An initial estimate of the correlation length  $a$  is obtained from the first zero-crossing of the autocorrelation function. Using these preliminary values of  $\nu$  and  $a$ , the best-fitting (in a least-squares sense) von Kármán autocovariance function (Eq. (6)) is found (dashed line).

these sediments can be estimated from compaction curves.

#### 4. Correlation structure of small-scale velocity fluctuations

In the following, we analyze the correlation structure of small-scale velocity fluctuations of the pertinent lithologies. For this purpose, Eq. (1) is modified to:

$$V(z) = V_0(z) + \sigma_V(z)s(z), \quad (5)$$

where  $V_0(z)$  is the large-scale deterministic trend and where  $\Delta V$  in Eq. (1) is replaced by  $\sigma_V(z)s(z)$  where  $\sigma_V(z)$  is the standard deviation of the stochastic small-scale fluctuations and  $s(z)$  are the normalized small-scale velocity fluctuations. Since  $V_0(z)$  and  $\sigma_V(z)$  have already been constrained for the various lithologies, we now seek to characterize  $s(z)$ . We shall assume that  $s(z)$  is a stationary random process, since the depth-variant components,  $V_0(z)$  and  $\sigma_V(z)$ , have been removed (Appendix B).

Because of the lack of sonic log data, density and porosity logs are also used to constrain  $s(z)$ . This approach is reasonable, because bulk density and porosity are directly related and because sonic velocity depends strongly on porosity (Fig. 11). Moreover, it is supported by the results of Dolan et al. (1998) and Leonardi and

Kümpel (1999), who analyzed the heterogeneity in the upper crust on the basis of various logs including P-wave, S-wave, bulk density, and neutron porosity. Their results indicate that statistical descriptions of

Table 6

Values of  $\nu$  and  $a$  for different lithologies, as determined from a variety of sonic, density, and porosity logs from the Iberia Abyssal Plain and Galicia margin

Site	Depth [m]	$\nu$	$a$ [m]	Lithology	Lith. Unit	Log type
1065	106–302	0.24	3.1	chalk, clay	II	<i>P</i> density
	107–284	0.27	2.8	chalk, clay	II	<i>P</i> porosity
	348–515	0.19	5.0	<sup>a</sup>	V.A	<i>S4</i> sonic
1068	515–599	0.40	3.7	<sup>b</sup>	V.B	<i>C6</i> sonic
	515–614	0.21	4.0	<sup>b</sup>	V.B	<i>C6</i> density
1068	142–442	0.23	7.5	chalk, clay	<sup>c</sup>	<i>P</i> density
	561–765	0.13	8.7	<sup>a</sup>	II	<i>S4</i> density
1069	105–765	0.18	14	<sup>a</sup>	II	<i>S4</i> density
	101–760	0.10	20	<sup>a</sup>	II	<i>S4</i> porosity
637	212–230	(0.1)	–	serpentinite		<i>M1</i> sonic
899	394–425	0.34	(1)	ophicalcite	IV.A	<i>M2</i> sonic
638	100–183	0.46	3.1	chalk	I	<i>P</i> sonic
637	100–212	0.32	2.4	<sup>a</sup>	I–III	<i>S4</i> density
639d	197–225	0.35	(1.1)	limestone	V	<i>C6</i> sonic
	197–265	0.39	1.2	limestone	V	<i>C6</i> density

The units given in column 6 correspond to the stratigraphic units as used in Boillot et al. (1987), Sawyer et al. (1994) and Whitmarsh et al. (1998). Numbers given in parenthesis are estimates obtained from short log intervals.

<sup>a</sup> Calcareous claystone, siltstone and sandstone.

<sup>b</sup> Dolomitic claystone, sandstone and conglomerate.

<sup>c</sup> Interval drilled, but not sampled; lithology inferred.

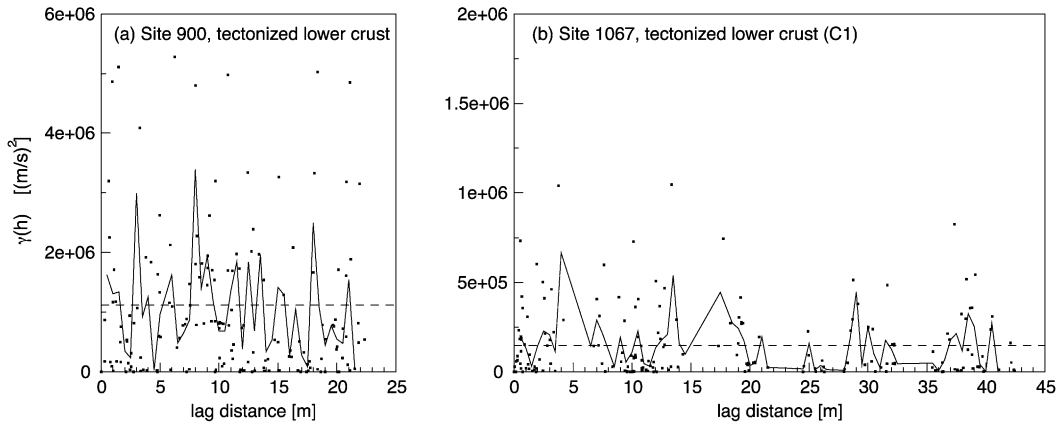


Fig. 13. Variograms of velocity laboratory measurements of the tectonized lower crustal basement (*CI*) at (a) Site 900 and (b) Site 1067. The squared differences in velocity are plotted against the distance of their sampling points (dots). Running mean for 0.5-m window length of these differences is shown by the solid line. No correlation at short lags can be identified. It is therefore concluded that the correlation length is likely to be some 2 m, which is the minimum analyzed lag. The dashed lines represent the variance of the data.

heterogeneity obtained from different log-types are similar. For lithological units for which sufficient data are not available, results from equivalent studies in the literature are used.

Depending on the spatial sampling density of the data (high-resolution log data versus lower resolution laboratory measurements) the analytical procedures differ. The obtained statistical characteristics are tested through stochastic simulations of sequences of small-scale fluctuations and qualitative comparison with corresponding observed data.

#### 4.1. Geophysical log data

Geophysical log data represent densely spaced (generally  $\Delta z = 0.1524 \text{ m} = 1/2 \text{ ft}$ ) in situ measurements of various petrophysical properties. Small-scale fluctuations in log data can be statistically characterized by their autocovariance function. Following Goff and Jordan (1988) and Holliger (1996), we used the von Kármán (1948) parametric model which characterizes Gaussian distributed random fields that are self-affine at scales smaller than the

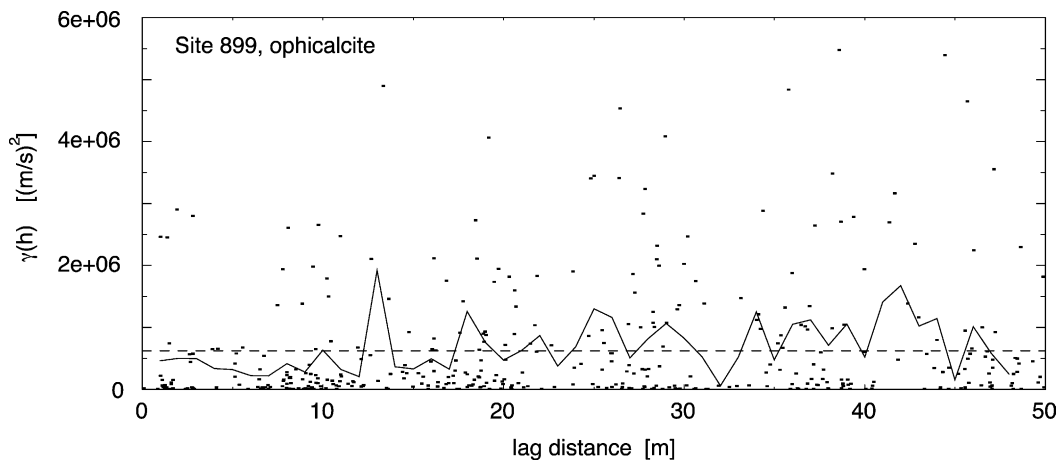


Fig. 14. Variogram cloud of velocity laboratory measurements in opicalcite at Site 899 (dots). Running mean (solid line) with a window length of 0.5 m indicates a correlation at distance shorter than 8–12 m. The variance of the process is represented by the dashed line.

correlation length  $a$ . The von Kàrmàn autocovariance function is given by:

$$C_{VV}(h) = \frac{\sigma^2}{2^{v-1}\Gamma(v)} \left(\frac{h}{a}\right)^v K_v\left(\frac{h}{a}\right), \quad (6)$$

where  $\Gamma$  is the gamma function,  $\sigma$  the standard deviation, and  $K_v$  the modified Bessel function of order  $0 \leq v \leq 1$ .  $v$  is related to the fractal dimension  $D$  (Mandelbrot, 1982) through  $D = E + 1 - v$  (Goff and Jordan, 1988) where the underlying  $E$  is the underlying Euclidean dimension (i.e.,  $E = 1$  in case of log data).  $D$  and  $v$  thus describe the roughness and complexity of the small-scale velocity variations:  $D = 1$ ,  $v = 1$  corre-

sponds to an optimally smooth fractal curve, whereas  $D = 2$ ,  $v = 0$  corresponds to an optimally rough fractal curve that essentially fills the 2D plane.

A common method to estimate  $v$  is to measure the roll-off rate of the power spectrum, i.e. the Fourier transform of the autocovariance function (e.g., Bendat and Piersol, 1986) of the data sequence. For von Kàrmàn-type stochastic processes, we obtain (e.g., Holliger, 1996):

$$\frac{d \log(P(k))}{d \log(k)} = -2v - E \quad (7)$$

for  $ka \gg 1$ .  $P(k)$  is the power spectrum and  $k$  is the wavenumber. This procedure is demonstrated on the

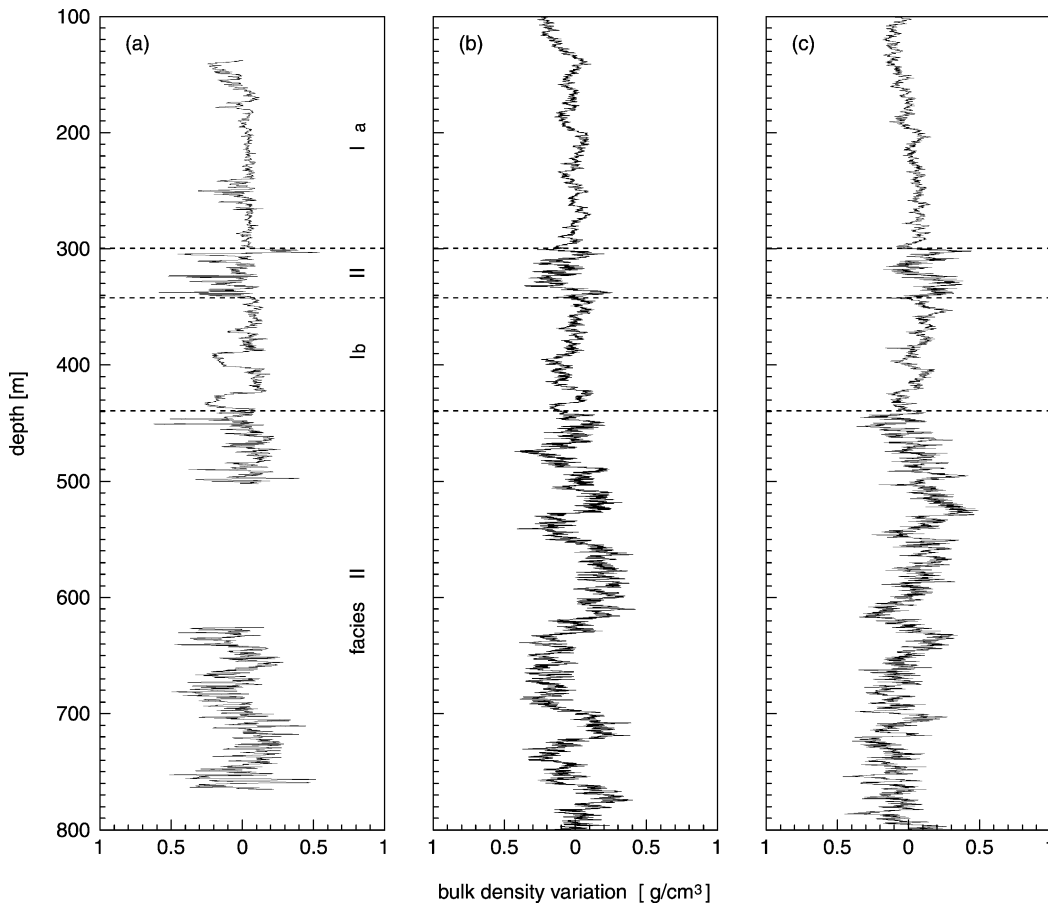


Fig. 15. Observed and simulated density fluctuations in post-rift sediments at Site 1068. The observed data (a) are compared with two realizations of synthetic data (b and c) in order to illustrate the viability of our stochastic model. The simulated data have the same second-order statistical properties as the observed data. Facies I is characterized by  $v = 0.23$  and  $a = 7.5$  m. Facies II:  $v = 0.13$  and  $a = 8.7$  m. Both facies are clearly distinguishable based on the roughness of the corresponding log data, which is quantified by the  $v$  value.

basis of a log from Site 1068 (Fig. 12a). The correlation length in Eq. (6) is initially estimated from the lag distance to the first zero-crossing of the experimental autocorrelation function. Finally, both parameters,  $\nu$  and  $a$ , are optimized by least-square fitting the von Kàrmàn autocovariance function to the experimental autocorrelation function of the data (Fig. 12b, Table 6). Estimates of the correlation length and their correlation with geological properties depend to some extent on the length of the data sequence and hence the physical interpretation of this parameter needs to

be addressed with some caution (Goff and Holliger, 1999).

#### 4.2. Laboratory measurements

Data from discrete laboratory measurements do not provide the necessary resolution to perform the above spatial correlation analysis. However, some constraints with regard to the correlation length can be obtained from the analysis of variograms (e.g., Wackernagel, 1998). The squared differences of each combination of

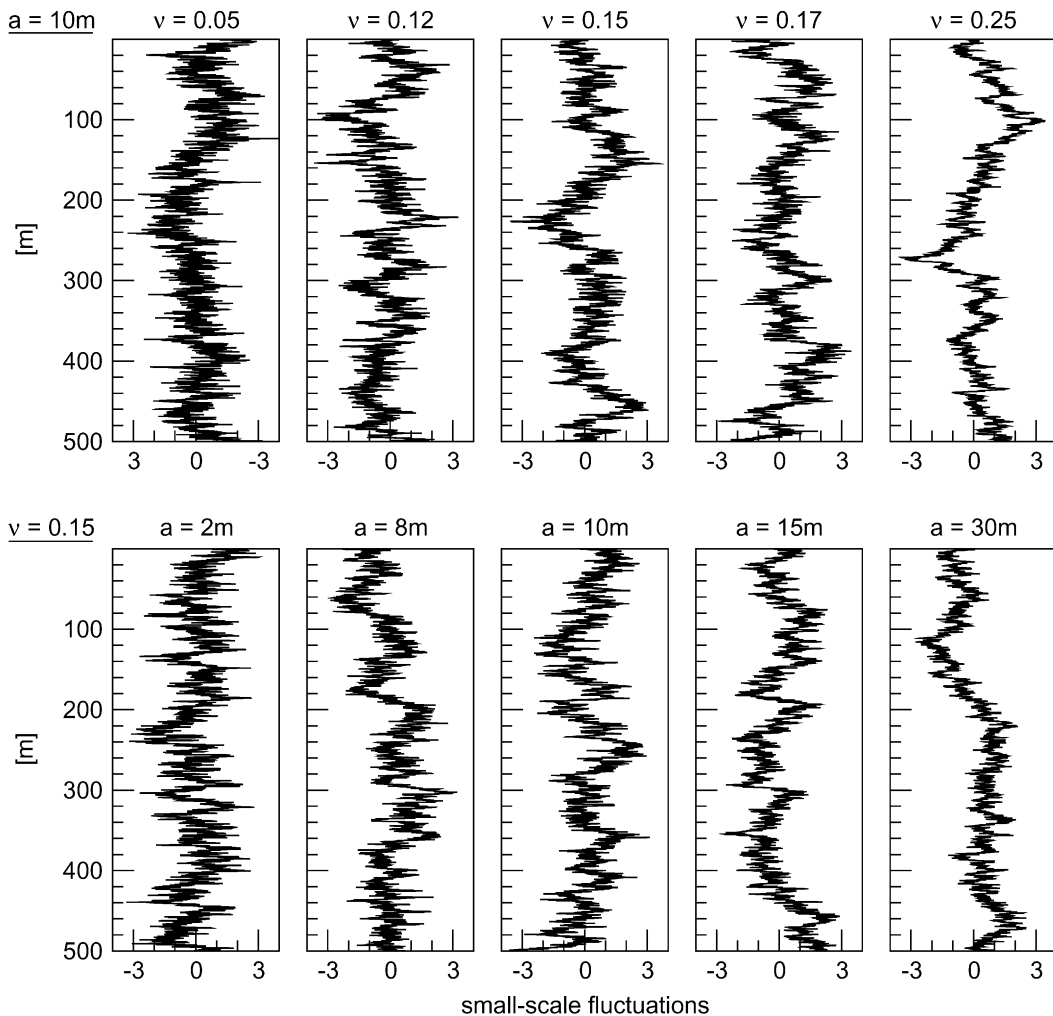


Fig. 16. Effects on the log character when varying  $\nu$  and  $a$ . The two central plots are characterized by the same  $\nu$  and  $a$ . All data sequences are based on different random data sequences and are normally distributed with  $\sigma = 1$ .

velocity measurements  $\gamma_{V_i V_j} = (V_i - V_j)^2$  were plotted against their distance in the borehole  $h = |z_i - z_j|$ . Running averages of the variogram cloud were calculated and investigated for correlation at small lag distance.

The variograms of velocity data from the lower crustal basement rocks (Fig. 13) at Sites 900 and 1067 do not indicate any correlation structure with a correlation length greater than approximately two m. This is compatible with the strong tectonization of these rocks. Since a value of  $\nu$  cannot be obtained from these data, we assume  $\nu = 0.1$ , based on the results of stochastic analyses presented by Holliger (1996) and Goff and Holliger (1999).

The variogram cloud of velocity data in opicalcite at ODP Site 899 (Fig. 14) shows a frequent occurrence of small velocity differences at small lags. The running mean of the variogram cloud stays below variance of the process at lag distances smaller than

10 m. Hence, a correlation length of approximately 10 m is assumed. This contradicts  $a = 1$  m, which was obtained from a sonic log at the same site (Table 6). However, the considered log interval was shorter (31 m) than the sequence of laboratory measurements (102 m) and is hence less reliable.

#### 4.3. Data from the literature

Because no log data are available from crustal basement lithologies (C2 to C4) at the Iberian sites, the stochastic parameters of the small-scale sonic velocity fluctuations in four boreholes penetrating Variscan upper crustal basement are adapted from Holliger (1996). Holliger obtained relatively uniform  $\nu$  values varying between 0.1 and 0.14, correlation length of 60–160 m, and standard deviations about 5% for granitic rocks.

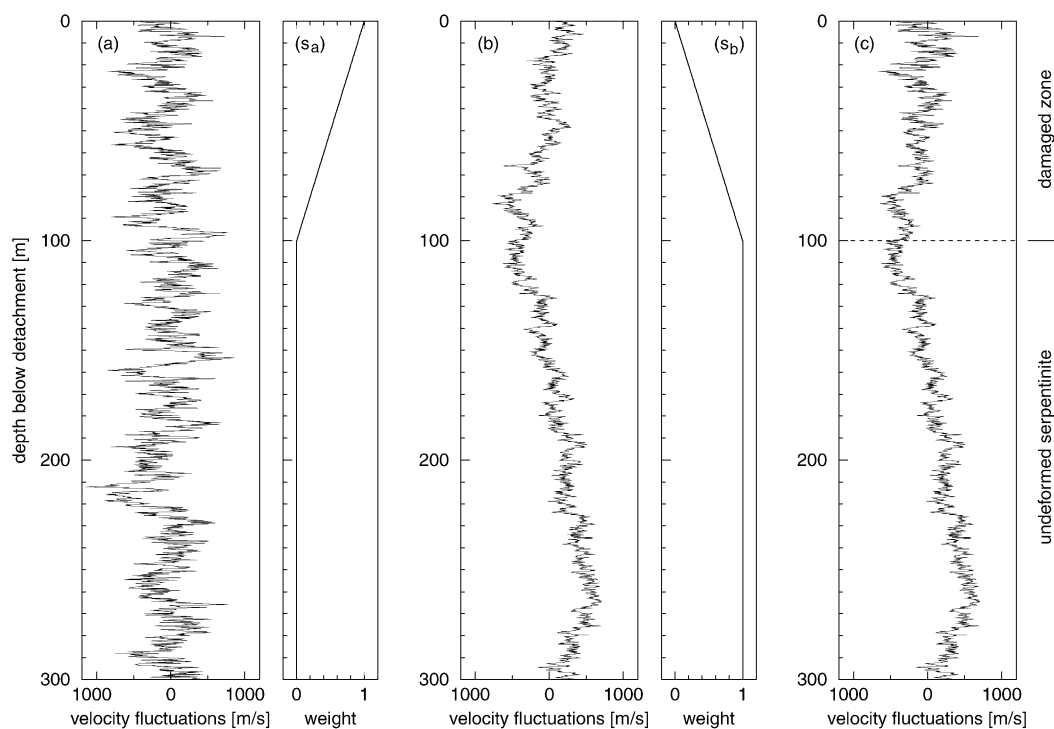


Fig. 17. Simulated velocity fluctuations for (a) cataclastically damaged serpentinite, (b) undeformed serpentinite, and (c) transition (upper 100 m) from damaged to undeformed serpentinite below a detachment fault. The transition was realized using a weight function ( $s$ ), where  $s_a + s_b = 1$ . The velocity fluctuations in the damaged zone are the sum of those in (a) and (b) each multiplied with the corresponding weight function:  $(c) = (s_a)(a) + (s_b)(b)$ . In this particular demonstration, the data sequences in (a) and (b) differ only in their correlation length:  $a = 2$  m in (a) and  $a = 100$  m in (b). Standard deviation and  $\nu$  are identical in both sequences ( $\sigma_V = 300$  m/s;  $\nu = 0.1$ ).

#### 4.4. Simulation of stochastic small-scale fluctuations

In order to validate the inferred values of  $v$  and  $a$ , synthetic data sequences were generated (Appendix C). The character of the synthetic data sequences is compared qualitatively with the small-scale fluctuations in the real log intervals. A comparison of real density fluctuations at Site 1068 with two realizations of synthetic data with identical second-order statistical properties is illustrated in Fig. 15. In this particular example, two facies (Ia/Ib and II) were identified in the observed data and then characterized by a different  $v$  value, correlation length and standard deviation. Facies Ia:  $v=0.23$ ,  $a=7.5$  m,  $\sigma_\rho=70$  kg/m<sup>3</sup>; facies Ib: as Ia, but  $\sigma_\rho=110$  kg/m<sup>3</sup>; facies II:  $v=0.13$ ,  $a=8.7$  m,  $\sigma_\rho=170$  kg/m<sup>3</sup>. We find that overall the character of the log data is indeed quite well reproduced by the synthetic data.

The effects of varying  $v$  and  $a$  are illustrated in Fig. 16. Starting points for this test are two sequences which are characterized by  $v=0.15$  and  $a=10$  m, which we find to be typical for the distal turbidite deposits in the Iberian margin (S4). The standard deviation  $\sigma$  in all examples is one. We find that varying  $v$  requires differences of about 0.05 to result in a qualitatively different character of the data sequence. In contrast, differences in the correlation scale are more difficult to discern. This is consistent with the ongoing debate about the nature and origin of this parameter (Goff and Holliger, 1999). The synthetic test logs are based on different random data sequences. Repeating the experiment with a constant initial seed for the random number generator does, however, lead to the same conclusions.

## 5. Seismic models

Based on the results from the previous sections, 1D velocity and density models of lithological profiles A through D (Figs. 2 and 3) are constructed and their seismic responses are evaluated. The primary objective is to explore the seismic responses from the shallow basement detachment structures which are the key tectonic features in the distal segment of magma-poor continental margins, and whose identification and interpretation in seismic reflection images still represents a major challenge.

#### 5.1. Construction of the seismic models

Velocity models of each lithological profile (Fig. 3) are constructed according to the concept summarized in Eq. (1): first the large-scale deterministic velocity–depth functions of the lithological units (Fig. 3) are assembled; then stochastic small-scale fluctuations are simulated for each lithological unit (Appendix C); finally, the small-scale velocity fluctuations are added to the large-scale model, resulting in one possible realization of the final velocity model. For comparison always two end-member realizations of velocity models for each lithological profile are shown in Figs. 18–21, whereby numerous realizations were simulated. The two end-member realizations are denoted as r1 and r2 and differ in only the random seed number used to generate the small-scale velocity fluctuations. For the corresponding density models only the large-scale density trend is considered because small-scale density fluctuations strongly correlate with small-scale velocity fluctuations (Sheriff and Geldart, 1995, p. 116ff) and hence do not fundamentally contribute to the complexity of the model.

A combination of two models with different statistical properties is necessary to realize the transition from cataclastic rocks to undeformed rocks in the uppermost serpentinite (M1) and in the cataclastic granites (C3), which is illustrated in Fig. 17.

The parameters of the velocity and density models are summarized in Tables 7 and 8. Whereas for Profiles A and B all parameters are obtained from the Iberian sites, the parameters for Profile C and D are compiled jointly from the Alpine sites, the Iberian sites and the pertinent literature (Holliger, 1996). In all models the water has a depth of 4000 m, a sonic velocity of 1500 m/s, and a density of 1000 kg/cm<sup>3</sup>.

For each lithological profile, the corresponding velocity and density models are converted into 1D synthetic seismograms. This is achieved by calculating the reflection coefficients as a function of depth, conversion of depth to two-way travel time, and convolution with zero-phase Ricker wavelets with peak frequencies of 15, 30, and 45 Hz, respectively. The bandwidth of these seismic wavelets is about two to three octaves and thus comparable to that of most upper crustal seismic reflection surveys.

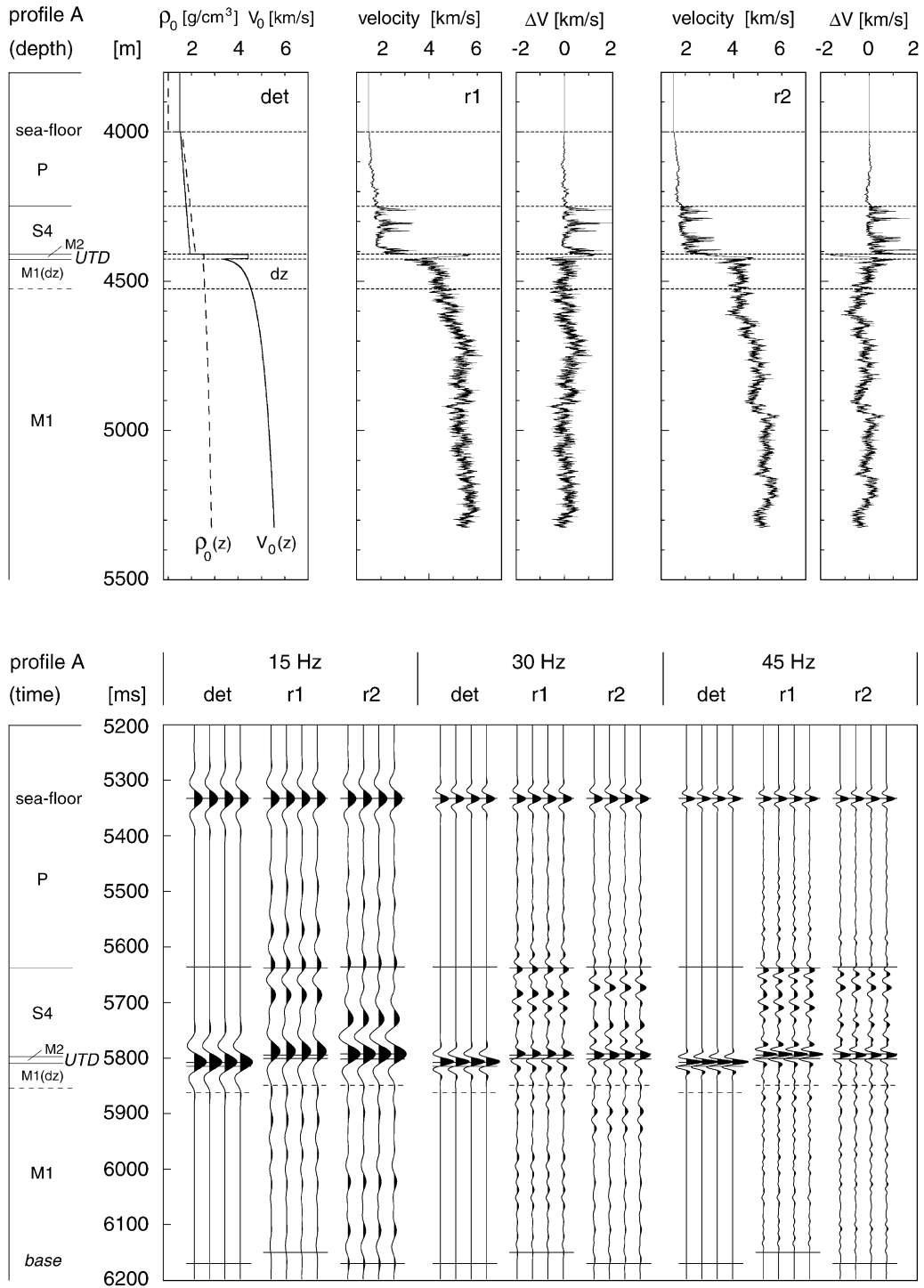


Fig. 18. Velocity and density models and resulting synthetic seismograms of Profile A. The models based only on the deterministic large-scale trends are denoted as det, those including stochastic small-scale velocity fluctuations are identified as r1 and r2.

## 5.2. Seismic models of two key locations in an OCT

### 5.2.1. Profile A: exhumed mantle detachment

In Profile A, the *UTD* (Upper Tasna Detachment) exhumes mantle rocks. Accordingly, the fault plane represents the sediment–basement contact and is associated with substantial jumps in velocity and density. The latter finds its expression in a large reflection coefficient and a correspondingly prominent seismic reflection (Fig. 18). However, the *UTD* is not a discrete seismic velocity interface, but rather a transition resulting from the downward decreasing fracture density of the uppermost mantle rocks (*MI*). Hence, the strength of a reflection from the *UTD* depends on the velocity gradient in this damaged zone and therefore on its laterally varying thickness. In contrast, the variable nature of the thin ophicalcite layer (*M2*), as apparent in the two realizations of the velocity model (Fig. 18), does not appear in the seismic response of the *UTD*. Since the ophicalcite is a discontinuous layer of strongly varying thickness, it might, however, result in diffracted waves in a 2D profile.

Two additional features in the synthetic seismograms are worth noting: (i) reflections in the sedimentary cover are relatively weak compared with the reflection from the *UTD*; (ii) small-scale velocity fluctuations in the sediments cause travel time shifts up to 30 ms on the time-position of the *UTD*. The latter is an effect of the log-normal distribution of small-scale velocity fluctuations in the *S4* sediments, whose arithmetic mean is shifted with respect to the large-scale trend.

### 5.2.2. Profile B: exhumed continental detachment and continent–mantle detachment

In Profile B, the *UTD* and the *LTD* (Lower Tasna Detachment) enclose a wedge of strongly tectonized lower crustal rocks (*CI*), which have a high mean velocity and a strong velocity variability (Table 7, Fig. 19).

A positive reflection is present from the *UTD*, which again represents the sediment–basement contact. In contrast to the *UTD* in Profile A, the impedance contrast is even stronger and is not expected to vary laterally because of the overall homogeneously healed fracture porosity in the lower crustal rocks (*CI*) forming the footwall. The seismograms in Fig. 19 show that

Table 7

Parameters of the velocity and density models of Profiles A and B

Unit	Lithology	$V_0$ [m/s]	$\sigma_V$ [m/s]	$a$ [m]	$v$	$\rho_0$ [kg/m <sup>3</sup> ]
<i>P</i>	clay, ooze	$z + 1530$	$0.3z + 10$	3.5	0.3	$1.4z + 1600$
<i>S4</i>	calc. siltstone	$z + 1530$	<sup>a</sup>	10	0.18	$1.4z + 1600$
<i>SI</i>	breccia	4889	819	1	0.1	2630
<i>CI</i>	<sup>b</sup>	5700	750	2	0.1	2780
<i>M2</i>	ophicalcite	4437	737	6	0.3	2540
<i>MI(dz)</i>	serpentinite	<sup>c</sup>	<sup>c</sup>	2	0.1	<sup>c</sup>
<i>MI</i>				100		

*dz* cataclastically deformed serpentinite in the damaged zone.

<sup>a</sup> Log-normal distribution of  $\Delta V$  with  $\mu_y = 6.5$  and  $\sigma_y = 0.8$ , which was finally shifted by  $-160$  m/s:  $V = V_0 + \Delta V - 160$ .

<sup>b</sup> An assemblage of amphibolites, gabbros and tonalites.

<sup>c</sup> See Fig. 5, Table 2 and Eqs. (2) and (3).

it is actually the contrast between the post-rift sediments (*S4*) and the thin layer of well lithified polymictic breccias (*SI*) that causes the reflection representing the *UTD* in the seismic data.

The *LTD* itself represents a prominent fast-to-slow velocity interface. Below the *LTD* a gradual slow-to-fast transition represents the damaged zone in the uppermost mantle rocks. An interesting feature of the corresponding seismic models is the frequency dependence of their seismic response. The 15-Hz seismograms (Fig. 19) image a positive reflection below the actual position of *LTD*, which represents the transition from cataclastically deformed to undeformed serpentinite. Conversely, the 30- and 45-Hz seismograms image the *LTD* itself as a negative reflection.

## 5.3. Seismic models of two key locations in the distal margin

### 5.3.1. Profiles C: crustal detachment

The large-scale structure of the Err detachment does not exhibit an impedance contrast, since syn-tectonic fracture healing causes the faulted rocks and the undeformed granites to have similar average velocities (Fig. 20). Also, the change in the nature of the small-scale velocity fluctuations occurring at the Err detachment does not cause any clear seismic reflections (Fig. 20). The most prominent feature in Profile C is the set of the strong reflections result-

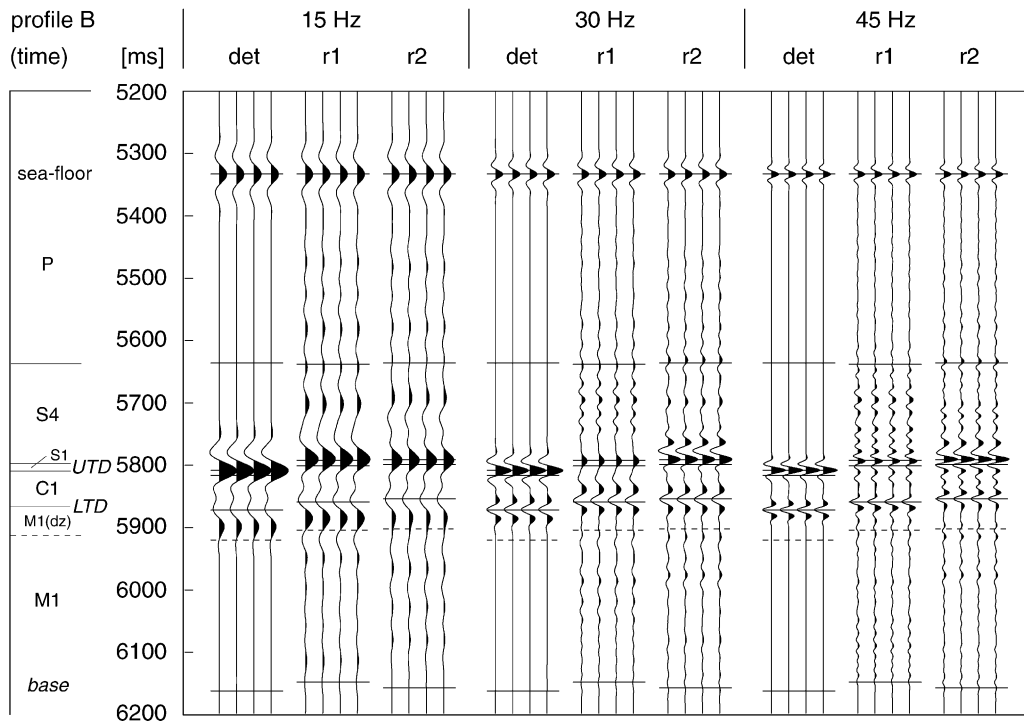
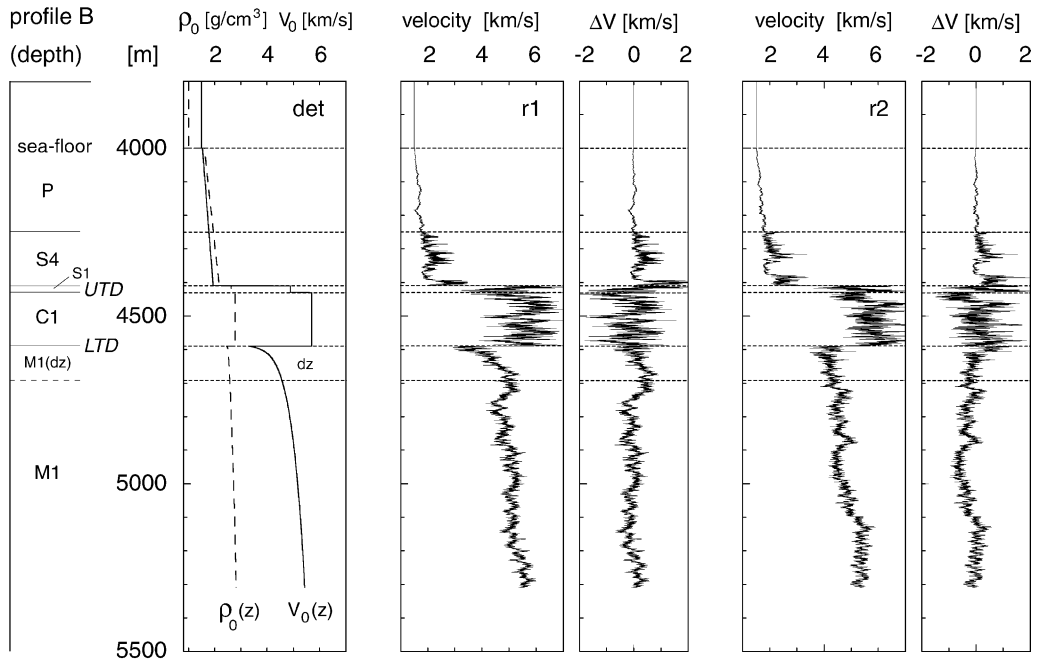


Fig. 19. Velocity and density models and resulting synthetic seismograms of Profile B. The models based only on the deterministic large-scale trends are denoted as det, those including stochastic small-scale velocity fluctuations are identified as r1 and r2.

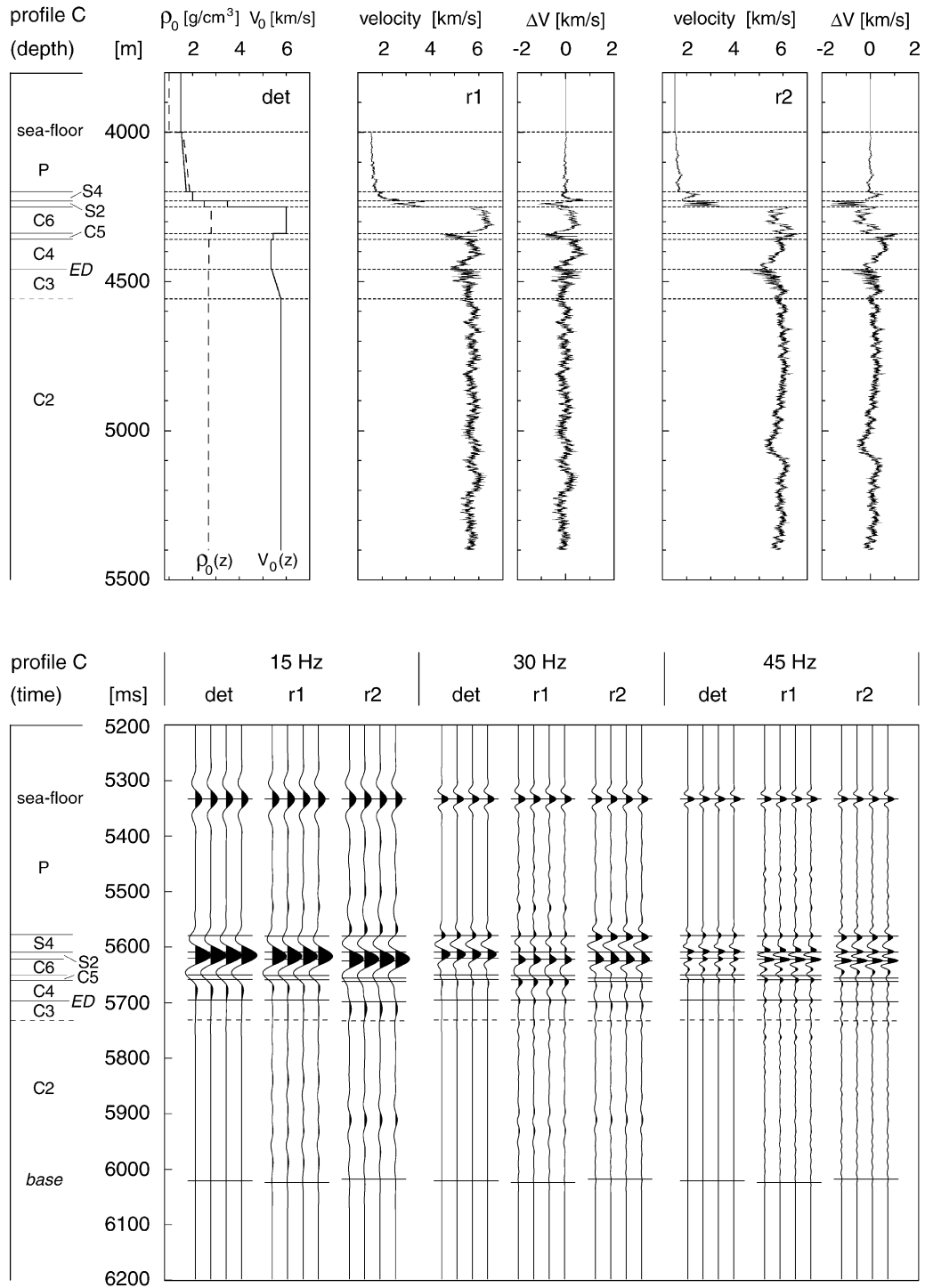


Fig. 20. Velocity and density models and resulting synthetic seismograms of Profile C. The models based on the deterministic large-scale trends only are denoted as det, those including stochastic small-scale velocity fluctuations are identified as r1 and r2. ED denotes the Err detachment.

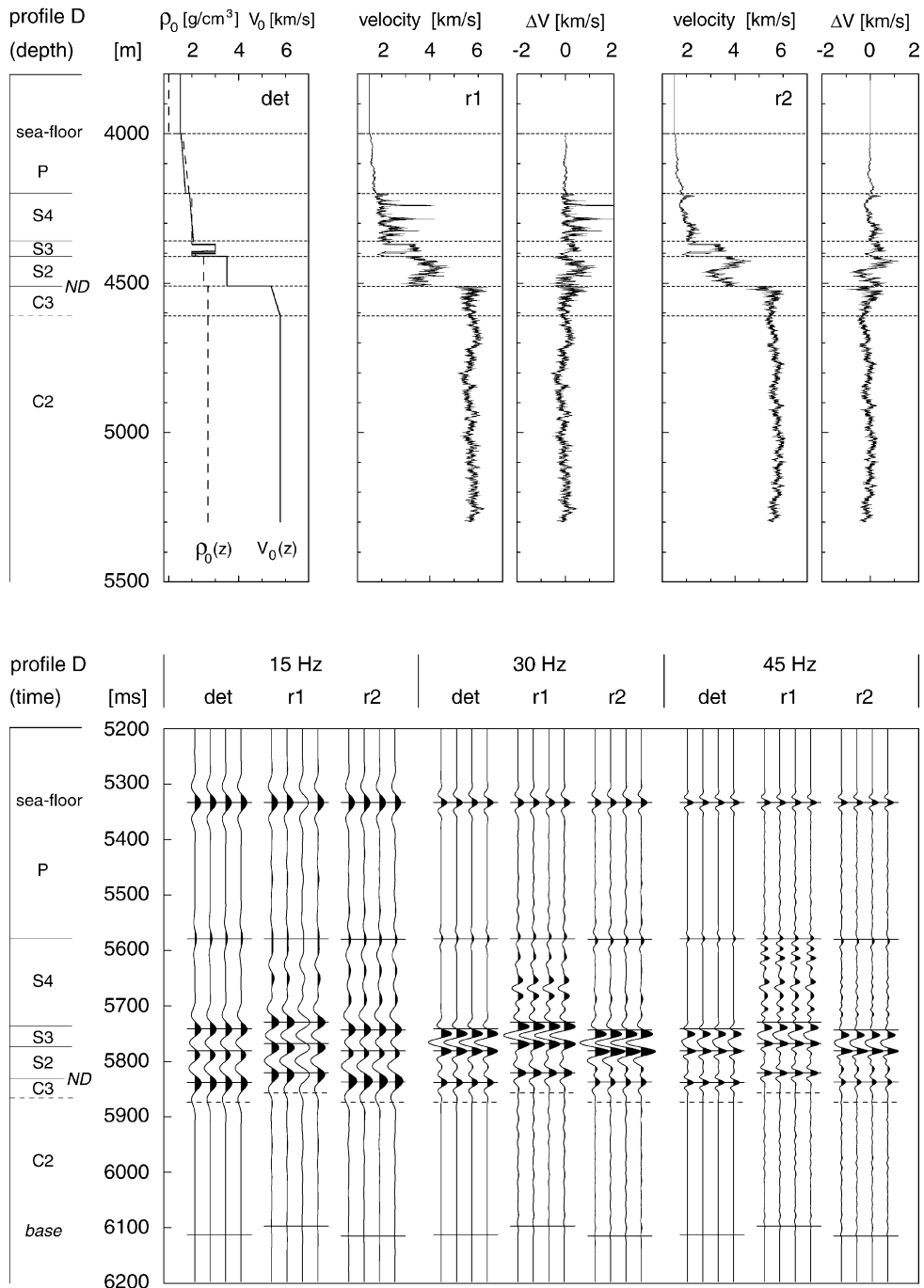


Fig. 21. Velocity and density models and resulting synthetic seismograms of Profile D. The models based only on the deterministic large-scale trends are denoted as det, those including stochastic small-scale velocity fluctuations are identified as r1 and r2. ND denotes the breakaway at Piz Nair.

ing from the syn- and pre-rift sedimentary interfaces.

### 5.3.2. Profiles D: exhumed breakaway of a crustal detachment

The breakaway of the detachment system at Piz Nair in Profile D (Fig. 3) exhumes cataclastically deformed upper crustal basement rocks (C3). The fault at Piz Nair is overlapped by syn-rift breccias (S2) and thus is also a sediment–basement contact. In the seismic velocity model it is represented by the lowermost slow-to-fast transition. Since the velocity structure of the basement in the footwall is relatively homogeneous, the synthetic seismograms do not show significant reflections (Fig. 21).

The turbidite formations S3 and S4 in Profile D are both characterized by the occurrence of unlithified and lithified strata. To take this into account, two different concepts are applied: (i) S4 is characterized by mainly soft sediments, interbedded with some lithified strata, whereby the degree of lithification varies. To include the higher velocities of the lithified strata, log-normally distributed velocity fluctuations are superimposed on the large-scale velocity trend of the soft sediments. (ii) S3 is characterized by different interbedded lithologies with more gradual changes. The interbedding of contrasting clay and sand layers is

taken into account in the large-scale velocity model (Fig. 21) and small-scale velocity fluctuations differ in the soft and lithified layers, as described in Table 8 (see facies S3a and S3b).

### 5.4. Comparison of the models with observed seismic data

A comparison of the seismic responses from models A and B (Figs. 18 and 19) with traces extracted from the seismic profile Lusigal 12 at Sites 1067 and 1068 (Krawczyk et al., 1996) shows remarkable similarities (Figs. 2a, 4 and 22).

Particularly striking are the similarities between the Lusigal 12 traces from Site 1067 and the seismic response of model B. The *HHD* at 7.6 s is imaged by a strong reflection overlain by weaker reflections from the sedimentary cover. A second reflection 200 ms below the *HHD* is of inverse polarity and hence indicative of a fast-to-slow interface. In analogy to the *LTD* in model B, we thus interpret this reflection as possibly representing the inferred *HD*.

The seismic response of the *HHD* at Site 1068 is more complex than that of model A. We attribute this to the syn-tectonic breccias which do not occur in Profile A (compare Figs. 3 and 4). Decisive for our hypothesis of Site 1068 and Profile B representing

Table 8  
Parameters of the velocity and density models of Profiles C and D

Unit	Lithology	$V_0$ [m/s]	$\sigma_V$ [m/s]	$a$ [m]	$v$	$\rho_0$ [kg/m <sup>3</sup> ]
<i>P</i>	clay, ooze	$z + 1530$ (I)	$0.3z + 10$ (I)	3.5 (I)	0.3 (I)	$1.4z + 1600$ (I)
<i>S4</i>	calc. siltstone	$z + 1700$ (Im)	(1)	10 (I)	0.18 (I)	2000 (I)
<i>S3b</i>	sandstone	3000 (Im)	300 (Im)	10 (e)	0.2 (e)	2660 (I)
<i>S3a</i>	clay	1900 (I)	120 (I)	10 (e)	0.2 (e)	2140 (I)
<i>S2</i>	breccias	3500 (e)	400 (Am)	5 (e)	0.2 (e)	2500 (e)
<i>C6</i>	dolomite	6000 (Am)	260 (A)	4 (I)	0.4 (I)	2810 (A)
<i>C5</i>	sandstone	5452 (A)	330 (A)	5 (e)	0.2 (e)	2650 (A)
<i>C4</i>	gneiss	5345 (A)	300 (Am)	60 (L)	0.14 (L)	2710 (A)
<i>C3</i>	cataclasite	5385 (A)	374 (A)	2 (e)	0.1 (e)	2690 (A)
<i>C2</i>	granite	5780 (A)	180 (A)	80 (L)	0.12 (L)	2680 (A)

(A) Based on data from Alpine sites.

(Am) Based on data from Alpine sites, modified.

(I) Based on data from Iberian sites.

(Im) Based on data from Iberian sites, modified.

(L) From Holliger (1996).

(e) Estimated.

(1) Log-normal distribution of  $\Delta V$  with  $\mu_y = 5.7$  and  $\sigma_y = 0.6$ , which was finally shifted by  $-300$  m/s:  $V = V_0 + \Delta V - 300$ .

$z$  refers to depth below the seafloor [m].

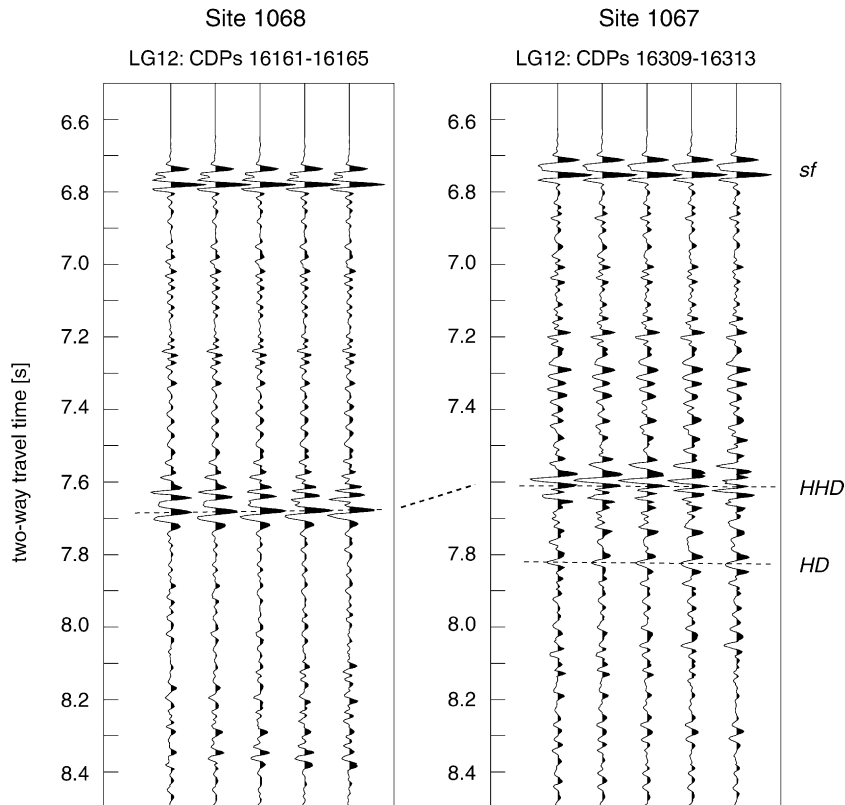


Fig. 22. Traces extracted from the Lusigal 12 profile (time migrated section processed by C.M. Krawczyk; courtesy of T. Reston, Geomar, Kiel) at Sites 1067 and 1068. The frequency content of the seismograms ranges from about 15 to 55 Hz and thus compares well with that of the 30 Hz synthetic seismograms of Profiles A and B (Figs. 18 and 19). It should, however, be noted that there are significant differences in the source wavelets of the synthetic and observed data. In particular, the source wavelets in the observed data are “mixed-phase” and exhibit a reverberatory character. At Site 1067, a reflection similar to that from the *LTD* in Profile B can be observed below the *HHD*. We interpret this reflection as imaging the proposed *HD* as shown in the lithological profile of Site 1067 (Fig. 4). *HHD* denotes the estimated two-way travel time to the Hobby High Detachment, *HD* the two-way travel time to the H-Detachment, and *sf* the reflection from the sea floor.

equivalent tectonic settings is the observation that there are no significant reflections below the *HHD*.

## 6. Discussion and conclusions

Shallow low-angle detachment faults are key tectonic features in the distal segments of magma-poor rifted continental margin and hence the seismic imaging of such features in present-day passive margins has been a major focus of research. The identification and characterization of such detachment faults in the seismic data from present-day rifted margins is, however, generally difficult and ambiguous. We have attempted to alleviate this problem by studying vari-

ous settings of shallow to top-basement level detachment faults in spectacularly exposed and geologically well-constrained remnants of the fossil Tethyan magma-poor rifted continental margin. The types of detachment faults examined include: exhumed mantle rocks, exhumed lower crustal rocks, juxtaposed crustal and mantle rocks, and an shallow crustal detachment separating gneisses and granites (Figs. 2 and 3). Along these faults variable velocity and density contrasts are observed, which we largely attribute to the different fracture-healing behavior in crustal and mantle rocks.

In crustal rocks, early syn-tectonic fracture healing results in a high average seismic velocity and a relatively homogenous velocity structure. Therefore, shal-

low intra-crustal detachment faults, as present in Profile C, appear to be seismically undetectable features. Detachment faults exhuming crustal rocks (see Profile D and the *UTD* in Profile B) are characterized by prominent slow-to-fast transitions in the velocity–depth function. In mantle rocks a significant fracture density associated with the detachment faults remains unhealed after rifting and results in a prominent low velocity zone. Such low velocity zones are crucial for the potential of seismic methods to image the faults. In case of exhumed mantle detachments (*UTD* in Profile A) and crust–mantle detachments (*LTD* in Profile B) the modeled seismic response is variable and depends on the thickness of the damaged zone and the frequency content of the seismic signal.

Accounting for small-scale velocity fluctuations has allowed us to construct 1D seismic models and synthetic seismograms of unprecedented realism and has provided valuable insights into the complex nature of the seismic response of passive continental margins. For example, in the case of the crustal Err detachment it is only the contrasting nature of the small-scale heterogeneities in the hanging wall and footwall, which causes a discernible reflection.

This study has concentrated on selected profiles from pertinent sites in the present-day Iberian and fossil Tethyan margins. A careful synoptic approach has allowed to construct detailed 1D seismic models and provided valuable insight into whether and how low-angle detachment faults might be discernible in seismic images of magma-poor continental margins.

### Acknowledgements

This work has been financed by the Swiss Federal Institute of Technology (ETH Project 0-20511-98) and associated with the Swiss National Science Foundation project “Comparative anatomy of passive continental margins: Iberia and Eastern Alps” (No. 20-055284-98). We thank D. Bernoulli for stimulating discussions and for critically reading this manuscript, and L. Burlini (ETH Zurich), G. Eberli (RSMAS Miami), and X. Janson (RSMAS Miami) for help with the laboratory work. The laboratory measurements were carried out at the Rock Deformation Laboratory of ETH Zurich and at the Petrophysics Laboratory of RSMAS Miami.

### Appendix A. A laboratory methods

The laboratory work for this study was carried out at the Petrophysics Laboratory of the University of Miami, FL, USA, and at the Rock Deformation Laboratory at ETH, Zurich, Switzerland.

Compressional wave velocities, shear wave velocities, connected porosities, and bulk densities were obtained from measurements on cylindrical mini-plugs. These miniplugs (minicores) are 1 in. (2.54 cm) in diameter and 3–5 cm long. Their ends were ground parallel within  $\pm 0.02$  mm and the samples were dried overnight at a temperature of 60 °C.

Core dimensions, weight, and effective pore volume were measured on the dry plug at room temperature. Pore volume measurements were performed using a helium pycnometer. Bulk density  $\rho_{\text{bulk}}$  was calculated assuming a pore fluid density  $\rho_{\text{fluid}}$  of 1000 kg/m<sup>3</sup> in order to simulate a water-saturated stage:

$$\rho_{\text{bulk}} = \frac{m + v_{\text{pore}}\rho_{\text{fluid}}}{v_{\text{plug}}} \quad (\text{A.1})$$

where  $m$  is the mass of the dry plug and  $v_{\text{pore}}$  and  $v_{\text{plug}}$  are the plug volume and the pore volume, respectively. After those measurements the dry sample was water-saturated under under-pressure overnight.

Sonic velocities of a compressional wave and two perpendicularly polarized shear waves were measured on the water-saturated samples using the pulse transmission technique (Birch, 1960). The dominant pulse frequency for these measurements was 1 MHz. First, only the compressional wave velocity was measured on the plain sample at room temperature and atmospheric pressure. In the following the sample was jacketed and placed into a pressure vessel. Compressional wave velocities were measured at independently controlled pore-fluid pressure (internal stress) and confining pressure (external stress) conditions. According to Coyner (1984), sonic velocity dependence on pressure can be adequately described by effective or differential stress only, which is defined as the difference between external and internal stress. Combinations of internal stress varying between 2 and 10 MPa and external stress varying from 5 to 105 MPa were realized. All measurements were performed while increasing the effective stress, resulting in velocity measurements as a function of effective pressure. A detailed description

of the experimental procedure is given by Christensen (1985).

### Appendix B. Stochastic analysis of the velocity and density data

Analysis of the correlation structure of small-scale velocity and density fluctuations assumes the data to be stationary. To achieve this, a large-scale trend is removed from the data. The residual data are then tested for stationarity in variance, by evaluating the standard deviation in a moving window (Fig. 9). If standard deviation is significantly varying with depth, a model relating standard deviation to depth  $\sigma_V(z)$  is established and the small-scale fluctuations  $\Delta V(z)$  are normalized as

$$s(z) = \frac{\Delta V(z)}{\sigma_V(z)}. \quad (\text{B.1})$$

Several lithological units are so thin that physically meaningful trends of velocity or density with depth can not be identified. In such cases, the data are assumed to be stationary and consequently a constant  $\bar{V}$  and  $\sigma_V$  are determined for each of those units (Table 6).

### Appendix C. Simulation of stochastic small-scale fluctuations

The reverse of the analytical procedure as outlined in Section 4 can be used to generate synthetic data sequences which are characterized by a particular  $v$  value, correlation length  $a$  and variance  $\sigma^2$ . The power spectrum corresponding to the autocorrelation model in Eq. (6) is given by (e.g., Holliger, 1996):

$$P(k) = \frac{\sigma^2(2\sqrt{\pi}a)^E \Gamma(v + E/2)}{\Gamma(v)(1 + k^2a^2)^{v+E/2}}, \quad (\text{C.1})$$

where  $k$  is the wavenumber,  $\Gamma$  is the gamma function, and  $E$  is the underlying Euclidean dimension which is equal to 1 in our case. The spectrum was calculated normalized to unit variance and is thus fully quantified by  $a$  and  $v$ . To generate a synthetic data sequence, the amplitude spectrum is calculated for the considered  $v$  value and correlation length  $a$  as  $\sqrt{P(k)}$ . This spectrum is then multiplied by a random phase factor  $\exp(i\Phi)$

with  $\Phi$  varying randomly and uniformly between  $-\pi$  and  $\pi$ . The thus resulting one-sided Fourier spectrum is mirrored and concatenated to yield an even spectrum. Taking the inverse Fourier transform yields one possible realization of the desired stochastic process, which is finally scaled to the desired standard deviation.

### References

- Bendat, J.S., Piersol, A.G., 1986. *Random Data, Analysis and Measurement Procedures*. Wiley, New York.
- Bertotti, G., Picotti, V., Bernoulli, D., Castellarin, A., 1993. From rifting to drifting: tectonic evolution of the south-Alpine upper crust from the Triassic to the Early Cretaceous. *Sediment. Geol.* 86, 53–76.
- Bertotti, G., Seaward, D., Wijbrans, J., ter Voorde, M., Hurford, A., 1999. Crustal thermal regime prior to, during, and after rifting: a geochronological and modeling study of the Mesozoic South Alpine rifted margin. *Tectonics* 18, 185–200.
- Beslier, M.-O., 1996. Seismic line LG12 in the Iberia Abyssal Plain. In: Whitmarsh, R.B., Sawyer, D.S., Klaus, A., Masson, D.G. (Eds.), *Proceedings of the Ocean Drilling Program: Scientific Results*. Vol. 149. ODP (Ocean Drilling Program), College Station, TX, pp. 737–740.
- Birch, F., 1960. The velocity of compressional waves in rocks to 10 kilobars. *J. Geophys. Res.* 65, 1083–1102, part 2.
- Boillot, G., Winterer, E.L., Meyer, A.W. et al., 1987. *Proceedings of the Ocean Drilling Program, Initial Reports*, Vol. 103. ODP (Ocean Drilling Program), College Station, TX.
- Boillot, G., Winterer, E.L. et al., 1988. *Proceedings of the Ocean Drilling Program: Scientific Results*, Vol. 103. ODP (Ocean Drilling Program), College Station, TX.
- Boillot, G., Beslier, M.-O., Krawczyk, C.M., Rappin, D., Reston, T.J., 1995. The formation of passive margins: constraints from the crustal structure and segmentation of the deep Galicia margin, Spain. In: Scrutton, R.A., Stoker, M.S., Shimmield, G.B., Tudhope, A.W. (Eds.), *The Tectonics, Sedimentation and Palaeo-oceanography of the North Atlantic Region*, vol. 90. Geological Society, London, Spec. Publ., pp. 71–91.
- Burke, M.M., Fountain, D.M., 1990. Seismic properties of rocks from an exposure of extended continental crust—new laboratory measurements from the Ivrea Zone. *Tectonophysics* 182, 119–146.
- Chian, D., Loudon, K.E., Minshull, T.A., Whitmarsh, R.B., 1999. Deep structure of the ocean–continent transition in the southern Iberia Abyssal Plain from seismic refraction profiles: Ocean Drilling Program (Legs 149 and 173) transect. *J. Geophys. Res.* 104, 7443–7462.
- Christensen, N.I., 1985. Measurements of dynamic properties of rock at elevated temperatures and pressures. In: Pincus, H.J., Hoskins, E.R. (Eds.), *Measurement of Rock Properties at Elevated Pressures and Temperatures*, vol. ASTM STP 869. American Society for Testing and Materials, West Conshohocken, PA, pp. 93–107.
- Coyner, K.B., 1984. effects of stress, pore pressure, and pore fluids on bulk strain, velocity and permeability in rocks. PhD thesis,

- Department of Earth, Atmospheric and Planetary Sciences, Massachusetts Institute of Technology.
- Dean, S.M., Minshull, T.A., Whitmarsh, R.B., Loudon, K.E., 2000. Deep structure of the ocean–continent transition in the southern Iberia Abyssal Plain from seismic refraction profiles: the IAM-9 transect at 40°20' N. *J. Geophys. Res.* 105, 5859–5885.
- Dolan, S., Bean, C.J., Riollet, B., 1998. The broad-band fractal nature of heterogeneity in the upper crust from petrophysical logs. *Geophys. J. Int.* 132, 489–507.
- Finger, W., 1978. Die Zone von Samaden (Unterostalpine Decken, Graub. unden) und ihre Jurassischen Brekzien. *Mitt. Geol. Inst. ETH Univ. Zürich*, p. 224.
- Florineth, D., Froitzheim, N., 1994. Transition from continental to oceanic basement in the Tasna nappe (Engadine window, Graub. unden, Switzerland): evidence for Early Cretaceous opening of the Valais ocean. *Schweiz. Mineral. Petrogr. Mitt.* 74, 437–448.
- Fountain, D.M., Hurich, C.A., Smithson, S.B., 1984. Seismic reflectivity of mylonite zones in the crust. *Geology* 12, 195–198.
- Froitzheim, N., Eberli, G.P., 1990. Extensional detachment faulting in the evolution of a Tethys passive continental margin, Eastern Alps, Switzerland. *Geol. Soc. Am.* 102, 1297–1308.
- Froitzheim, N., Manatschal, G., 1996. Kinematics of Jurassic rifting, mantle exhumation, and passive-margin formation in the Austroalpine and Penninic nappes (eastern Switzerland). *Geol. Soc. Am.* 108, 1120–1133.
- Froitzheim, N., Rubatto, D., 1998. Continental breakup by detachment faulting: field evidence and geochronological constraints (Tasna nappe, Switzerland). *Terra Nova* 10, 171–176.
- Goff, J.A., Holliger, K., 1999. Nature and origin of upper crustal seismic velocity fluctuations and associated scaling properties: combined stochastic analyses of KTB velocity and lithology logs. *J. Geophys. Res.* 104, 13169–13182.
- Goff, J.A., Jordan, T.H., 1988. Stochastic modeling of seafloor morphology: Inversion of sea beam data for second-order statistics. *J. Geophys. Res.* 93, 13589–13608.
- Hébert, R., Gueddari, K., Laflèche, M.R., Beslier, M.-O., Gardien, V., 2001. Petrology and geochemistry of exhumed peridotites and gabbros at non volcanic margins: ODP Leg 173 West Iberia ocean–continent transition zone. In: Wilson, R.C.L., Whitmarsh, R.B., Taylor, B., Froitzheim, N. (Eds.), *Non-Volcanic Rifting of Continental Margins: A Comparison of Evidence from Land and Sea*, vol. 187. Geological Society, London, Spec. Publ., pp. 161–189.
- Holliger, K., 1996. Upper-crustal seismic velocity heterogeneity as derived from a variety of p-wave sonic logs. *Geophys. J. Int.* 125, 813–829.
- Hurich, C.A., Fountain, S.B.S.D.M., Humphreys, M.C., 1985. Seismic evidence of mylonite reflectivity and deep structure in the Kettle dome metamorphic core complex, Washington. *Geology* 13, 577–580.
- Jones, T., Nur, A., 1982. Seismic velocity and anisotropy in mylonites and the reflectivity of deep crustal fault zones. *Geology* 10, 260–263.
- Kern, H., Richter, A., 1981. Temperature derivatives of compressional and shear wave velocities in crustal and mantle rocks at 6 kbar confining pressure. *J. Geophys. Res.* 49, 47–56.
- Krawczyk, C.M., Reston, T.J., Beslier, M.-O., Boillot, G., 1996. Evidence for detachment tectonics on the Iberia Abyssal Plain rifted margin. In: Whitmarsh, R.B., Sawyer, D.S., Klaus, A., Masson, D.G. (Eds.), *Proceedings of the Ocean Drilling Program: Scientific Results*. Vol. 149. ODP (Ocean Drilling Program), College Station, TX, pp. 603–615.
- Leonardi, S., Kumpel, H.J., 1999. Fractal variability in superdeep borehole; implications for the signature of crustal heterogeneities. *Tectonophysics* 301, 173–181.
- Manatschal, G., 1999. Fluid- and reaction-assisted low-angle normal faulting: evidence from rift-related brittle fault rocks in the Alps (Err Nappe, eastern Switzerland). *J. Struct. Geol.* 21, 777–793.
- Manatschal, G., Bernoulli, D., 1999. Architecture and tectonic evolution of nonvolcanic margins: present-day Galicia and ancient Adria. *Tectonics* 18, 1099–1119.
- Manatschal, G., Nievergelt, P., 1997. A continent–ocean transition recorded in the Err and Platta nappes (Eastern Switzerland). *Eclogae Geol. Helv.* 90, 3–27.
- Manatschal, G., Froitzheim, N., Rubenach, M.J., Turrin, B.D., 2001. The role of detachment faulting in the formation of an ocean–continent transition: insights from the Iberia Abyssal Plain. In: Wilson, R.C.L., Whitmarsh, R.B., Taylor, B., Froitzheim, N. (Eds.), *Non-volcanic Rifting of Continental Margins: A Comparison of Evidence from Land and Sea*, vol. 187. Geological Society, London, Spec. Publ., pp. 405–428.
- Mandelbrot, B.B., 1982. *The Fractal Geometry of Nature*. Freeman, New York.
- Mauffret, A., Montadert, L., 1987. Rift tectonics on the passive continental margins off Galicia (Spain). *Mar. Pet. Geol.* 4, 49–70.
- McCaffree, C.L., Christensen, N.I., 1993. Shear wave properties and seismic imaging of mylonite zones. *J. Geophys. Res.* 98, 4423–4435.
- Naef, H., 1987. Ein Beitrag zur Stratigraphie der Trias–Serien im Unterostalpin Graub. unden (Grisoniden). *Mitt. Geol. Inst. ETH Univ. Zürich*, 224.
- Reston, T.J., Krawczyk, C.M., Klaeschen, D., 1996. The S reflector west of Galicia (Spain): evidence from prestack depth migration for detachment faulting during continental breakup. *J. Geophys. Res.* 101, 8075–8091.
- Sawyer, D.S., Whitmarsh, R.B., Klaus, A., et al., 1994. *Proceedings of the Ocean Drilling Program, Initial Reports*. Vol. 149. ODP (Ocean Drilling Program), College Station, TX.
- Sheriff, R.E., Geldart, L.P., 1995. *Exploration Seismology*. Cambridge University Press, Cambridge.
- von Kármán, T., 1948. Progress in the statistical theory of turbulence. *J. Mar. Res.* 7, 252–264.
- Wackernagel, H., 1998. *Multivariate Geostatistics*. Springer Verlag, New York.
- Wepfer, W.W., Christensen, N.I., 1991. A seismic velocity–confining pressure relation, with applications. *Int. J. Rock Mech. Miner. Sci. Geomech. Abstr.* 28, 451–456.
- Whitmarsh, R.B., Beslier, M.-O., Wallace, P.J., et al., 1998. *Proceedings of the Ocean Drilling Program, Initial Reports*. Vol. 173. ODP (Ocean Drilling Program), College Station, TX.
- Whitmarsh, R.B., Dean, S.M., Minshull, T.A., Tompkins, M., 2000. Tectonic implications of exposure of lower continental crust beneath the Iberia Abyssal Plain, Northeast Atlantic Ocean: geophysical evidence. *Tectonics* 19, 919–942.